Solar Energy 228 (2021) 317–332

Contents lists available at ScienceDirect

Solar Energy

journal homepage: www.elsevier.com/locate/solener

Forecasting dust impact on solar energy using remote sensing and modeling techniques

Akriti Masoom [a,*], Panagiotis Kosmopoulos [b,*], Ankit Bansal [a], Antonis Gkikas [c], Emmanouil Proestakis [c], Stelios Kazadzis [d], Vassilis Amiridis [c]

[a] *Department of Mechanical and Industrial Engineering, Indian Institute of Technology Roorkee, Uttarakhand 247667, India*
[b] *Institute for Environmental Research and Sustainable Development, National Observatory of Athens (IERSD/NOA), Penteli, 15236 Athens, Greece*
[c] *Institute for Astronomy, Astrophysics, Space Applications and Remote Sensing, National Observatory of Athens (IAASARS/NOA), Penteli, 15236 Athens, Greece*
[d] *Physikalisch Meteorologisches Observatorium Davos, World Radiation Center (PMOD/WRC), CH-7260 Davos, Switzerland*

ARTICLE INFO

Keywords:
Solar irradiance
Solar energy
Dust impact
Ground-based measurements
Passive and active satellite observations
Aerosol and dust optical depth

ABSTRACT

The present study focuses on assessment of dust impact on forecasting solar irradiance and energy, during an extreme dust event. We utilize surface-based Aeronet measurements, satellite observations (MODIS and CALIPSO), and ModIs Dust AeroSol (MIDAS) dust database in conjunction with Weather Research and Forecasting (WRF) model simulations, based on inputs from Indian Solar Irradiance Operational System (INSIOS) and Copernicus Atmosphere Monitoring Service (CAMS) forecast. This work presents a novel approach of CAMS aerosol optical depth (AOD) ingestion into WRF model for analyzing dust impact on solar irradiance. The study region is the northwestern part of Indian subcontinent, an area with some of the largest solar power projects in India. A set of three consecutive and deadly dust storms occurred in May 2018 with one having high intensity and values of AOD and dust optical depth reaching up to 2. Dust events of this extent leads to a significant reduction in solar irradiance and affect the capacity of energy exploitation through Photovoltaic installations and Concentrating Solar Power plants due to the solar aerosol-related extinction. The dust plume resulted in an average decrease of 76 W/m^2 and 275 W/m^2 for global horizontal irradiance (GHI) and direct normal irradiance (DNI), respectively, and a maximum reduction of 100 W/m^2 (10%) and 400 W/m^2 (40%) in GHI and DNI, respectively. The proposed methodology can support solar energy producers, for optimum energy production forecasting, management, and maintenance (e.g. soiling) as well as transmission and distribution system operators, taking into account the effect of dust aerosols into their day-to-day market operations.

1. Introduction

The potential of solar energy exploitation is dependent on various atmospheric parameters such as clouds and aerosols that contribute to the attenuation of the incoming solar radiation reaching the Earth,s surface. Thus, large photovoltaic installations are built in regions of high solar insolation and year-round cloud-free sky conditions. The northwestern semi-arid region of India is a high solar insolation area with mostly clear skies throughout the year. However, the same region also witnesses occasional dust storms, related to long-range transport of high aerosol loads that block solar radiation (Masoom et al., 2020b) through aerosol absorption and scattering.

In Northern India, dust infiltrates the atmosphere through disturbed soils and wind erosion, attributed to hyper-arid, arid and semi-arid regions (Miller et al., 2004). In addition, the variation in the radiative impact of dust on different regions during long-range transport of dust is significant as it mixes with anthropogenic aerosols prevalent in the polluted areas (Deepshikha et al., 2005). The northern part of India is affected by pollution from various natural and anthropogenic emissions that deteriorate air quality that adversely affects the health of people (Du et al., 2016).

Dust storms frequently occur in the Gangetic Basin of Northern India every year during the pre-monsoon season, i.e., between March and June (Dey et al., 2004; Middleton, 1986). These dust storms are one of the major sources of pollution and their origin is traced back to the Thar desert and the Arabian Peninsula, where high heat prevails without much rainfall during the pre-monsoon season (Proestakis et al., 2018). Surface heating and a strong pressure gradient generate dust storms and westerly winds transport the ascending loose soil/sand particles

---

* Corresponding authors.

E-mail addresses: amasoom@me.iitr.ac.in (A. Masoom), pkosmo@noa.gr (P. Kosmopoulos), ankit.bansal@me.iitr.ac.in (A. Bansal), agkikas@noa.gr (A. Gkikas), proestakis@noa.gr (E. Proestakis), stelios.kazadzis@pmodwrc.ch (S. Kazadzis), vamoir@noa.gr (V. Amiridis).

https://doi.org/10.1016/j.solener.2021.09.033
Received 26 December 2020; Received in revised form 3 September 2021; Accepted 10 September 2021

over the Indian subcontinent (Sarkar et al., 2019). The dust rising from the Arabian Peninsula enters the Indian subcontinent either through Afghanistan and Pakistan track or via the Arabian Sea (Middleton, 1986). It is sometimes diverted to the Central parts of the Indian region depending upon the wind pattern (Kumar et al., 2015; Prasad and Singh, 2007) and leads to an enhancement of aerosol loading over the Indo–Gangetic Plain, affecting air quality and visibility (Sikka, 1997; Verma et al., 2013).

The Northwestern region of India experienced three major dust storms consecutively in May 2018 that led to loss of life and property, and adversely impacted human health and air quality. This series of dust storms started around April 26 and the first peak occurred on May 3, and dissipated a couple of days later (Sarkar et al., 2019). The origin of the dust storm is attributed to two different branches: One from the Arabian Peninsula, advected over India through western and southwestern regions by long-range transport and the other is attributed to the northwestern zones of Pakistan, Iran, and the Thar desert in India. The dust storm entered the Indian subcontinent through the western part, reached as far as Indo–Gangetic Plain, affecting major urban and rural areas, including Delhi, Rajasthan and western Uttar Pradesh. In the last three decades, the region of the Indo–Gangetic Plain had not experienced such a high magnitude of dust storms (Sarkar et al., 2019). The first dust storm peaked between May 2 and May 3 and affected the northern states of India comprising of Delhi, Rajasthan, Uttar Pradesh, and Haryana, injuring hundreds and claiming more than 125 lives. The second dust storm of the series prevailed from May 7 to May 8, and it did not cause many fatalities. The third dust storm occurred on the evening of May 12, and it claimed more than 30 lives. In this analysis, the dust storm of May 2 to May 3 was considered due to its severity and colossal impact. We have focussed the analysis on this particular dust case only in this work. Several studies like (Chakravarty et al., 2021; Kedia et al., 2018; Yuan et al., 2021; Aswini et al., 2020; Kosmopoulos et al., 2018b; Ohde and Siegel, 2012; Huang et al., 2019; Francis et al., 2021; Slingo et al., 2006) has been conducted dealing with one dust case. This is the reasonable way of analysis since the dust cases are different with different characteristics and impacts.

The absence of clouds makes dust the primary attenuator of solar radiation and affects more intensively the DNI than GHI (Kosmopoulos et al., 2018a). Several approaches have been used to quantify and estimate the impact of dust on solar radiation (Allen et al., 2013; Dirnberger et al., 2015; Lindfors et al., 2013; Papayannis et al., 2005; Qian et al., 2007). This analysis makes a step forward in this area by incorporating CAMS AOD directly into the WRF model to better understand the interaction between solar irradiance and the dust phenomenon. An assessment was made on the effect of strong dust events on solar energy with an analysis of three-day variation of AOD and solar irradiance using WRF and INSIOS models (Masoom et al., 2020a). The present study utilizes satellite and ground-based data for the estimation of the impact of an extreme dust event on the atmospheric radiative energy budget. The study region is confined to the northern part of the Indian subcontinent and several data sources were used to perform a multi-model analysis of the major dust storm between May 2 and May 4, 2018. The dust event was analyzed using the regional numerical weather prediction (NWP) model. NWP models are based on atmospheric physics and predicts the future atmospheric state using weather data and observations. WRF model is a mesoscale NWP model that has user-specific temporal and spatial resolution options. The parameterizations of the WRF model provide an opportunity to adapt the model configuration for the specific climatic condition (Masoom et al., 2019) and integrate the local observations and measurements enhancing the forecast accuracy. In this analysis, WRF mesoscale model was initialized with Global Forecast System (GFS), to forecast solar irradiance with high accuracy at the regional scale.

The data used include (i) NWP global model forecast from GFS and aerosol product of CAMS (Section 2.1.1), (ii) MODerate Resolution Imaging Spectroradiometer (MODIS) satellite aerosol retrievals and the MIDAS dataset (Section 2.1.2), (iii) aerosol profiling from Cloud-Aerosol Lidar Infrared Pathfinder Satellite Observation (CALIPSO) and LIdar climatology of Vertical Aerosol Structure for space-based lidar simulation studies (LIVAS) (Section 2.1.3), and finally, (iv) ground-based aerosol and irradiance retrievals procured from AErosol RObotic NETwork (Aeronet) sun photometers and Baseline Surface Radiation Network (BSRN) measurements (Section 2.1.4). The three-dimensional evolution of the dust outbreak was analyzed and its attenuation on the incoming solar radiation was calculated. A correlation was made within the available data so as to analyze the respective impact of aerosol on solar power. The analysis begins with an overview of the input data and the models in Section 2; Section 3 deals with the results from observations and ground measurements of the evolution of the dust event. The discussion of results is presented in Section 4 followed by conclusions in Section 5.

2. Data and methodology

2.1. Data

2.1.1. GFS and CAMS

The GFS data of National Oceanic and Atmospheric Administration available through the National Center for Environmental Protection (NCEP) and the CAMS Monitoring Atmospheric Composition and Climate (MACC) near real-time analysis were used to assess the meteorological conditions and analyze the evolution and transport of dust and its impact on solar radiation. The NCEP-GFS data is published at 00, 06, 12, and 18 UTC at a spatial and temporal resolution of $0.25^{\circ} \times 0.25^{\circ}$ on-grid and 3 h for the first 240 h (and 12 h for 240–384 h), respectively (NCEP, 2015). The analyses take into account the meteorological parameters like temperature, pressure, wind, geopotential height, etc.) at the surface, inside the boundary layer, and at pressure levels varying from 0.4 to 1000 mbar. For shortwave radiative transfer calculations, GFS uses the rapid radiative transfer model (Mlawer et al., 1997; Mlawer and Clough, 1998), which is based on correlated-k method for the transformation of radiative absorption coefficients (k) spectral dependence into a continuous cumulative distribution function. All vertical layers have independent radiative transfer calculations for each sub-interval which is performed by a two-stream adding method that corresponds to line-by-line radiative transfer model for individual spectral-point (Clough et al., 1992). It also takes into account the effect of absorption from water vapor, ozone, oxygen, and methane along with the contribution of the cloud optical depth, effective particle radius, asymmetry factor, and albedo to layer radiative properties. The primary dependence of cloud properties is on temperature, pressure, location, liquid water path, and ice water path (Hou et al., 2002) which is in similarity to the parameterization shown in Stephens and Greenwald (1991). In this analysis, the 00 UTC GFS data was used to initialize the WRF model to cover the peak time of the dust event.

The CAMS MACC near real-time forecast was used for better depiction of the dust event, and its transport. The CAMS forecasted AOD is based on the modeling of aerosol using European Centre for Medium-Range Weather Forecasts (ECMWF) physical parameterizations focusing on the aerosol processes (Benedetti et al., 2008; Morcrette et al., 2008; Reddy et al., 2005) and satellite data assimilation. MODIS AOD is assimilated into the database to exploit available information so as to evaluate the persistent bias from different data sources (Dee and Uppala, 2009). The database is available from 2012 at a spatial and temporal resolution of $0.4^{\circ} \times 0.4^{\circ}$ and 3 h, respectively (Engelen, 2018). The parameters include organic carbon, dust, black carbon, sea salt, and sulfates. We have used the CAMS AOD data initialized at 00 UTC to match with the synergy of the WRF model initialization. The uncertainty in the CAMS AOD forecast shows an average positive bias against the daily Aeronet level 1.5 data (Basart et al., 2019).

2.1.2. MODIS and MIDAS

The MODIS sensors onboard National Aeronautics and Space Administration (NASA) satellites Terra and Aqua (Salomonson et al., 1989) provide AOD retrievals at 550 nm. A pair of complementary algorithms, namely Deep Blue and Dark Target, are used over bright and arid land surfaces, and vegetated/dark land surfaces and the ocean, respectively (Levy et al., 2013). The daytime data acquisition time for Terra and Aqua are 05 UTC and 08 UTC (corresponding to the local time of 10:30 a.m. and 1:30 p.m., as IST is 5.5 h ahead of the Greenwich Mean Time). In this work, level-3 MODIS gridded atmosphere product (MOD08_D3) was utilized which contains daily-averaged values of cloud optical and physical properties, atmospheric aerosols, water vapor, total ozone burden, and atmospheric stability indices at a spatial resolution of $1^\circ \times 1^\circ$. The four level-2 MODIS atmosphere products are used to derive the level-3 MODIS atmosphere daily global parameters. MOD08_D3 product files are retrieved in Hierarchical Data Format from the LAADS web site (NASA, 2020).

In the current study, the dust optical depth (DOD) at 550 nm, obtained from the MIDAS dataset (Gkikas et al., 2021), has been utilized. The innovative and powerful elements of the MIDAS DOD includes its availability at fine spatial resolution ($0.1^\circ \times 0.1^\circ$) and on a global scale. This aspect is critical for depicting in detail the highly variable patterns of dust plumes, particularly under episodical conditions, above the sources as well as over downwind continental and maritime regions. The derivation of DOD is achieved through the multiplication of the MODIS-Aqua AOD (Levy et al., 2013) with the dust fraction (DF) to the total aerosol load, in optical terms, derived by the Modern-Era Retrospective analysis for Research and Applications (MERRA-2) reanalysis (Gelaro et al., 2017). In order to ensure the quality of the MIDAS DOD product, a series of quality filters have been applied to the raw MODIS AODs.

Moreover, the DF has been assessed thoroughly against the respective CALIPSO-based pure-dust product (Amiridis et al., 2013), derived by columnar integration of the quality assured (Marinou et al., 2017) Cloud-Aerosol Lidar with Orthogonal Polarization (CALIOP) vertical profiles, available from the LIVAS database (Amiridis et al., 2015). The reliability of the DF has been proven through the evaluation of the MIDAS DOD against Aeronet retrievals, in which the “contamination” of non-dust types has been minimized as much as possible, and its inter-comparison against MERRA-2 and LIVAS DODs has justified its validity. The MODIS-Aqua retrievals have been processed at the swath level (i.e. level 2), and they have been derived by the penultimate version (i.e., Collection 6) of the retrieval algorithm. Here, we are using the latest version (Collection 6.1) of the space-borne data, including also those obtained by the twin polar-orbit satellite (Terra) in which the MODIS spectroradiometer is mounted thus increasing the sampling throughout the day.

2.1.3. CALIPSO CALIOP and LIVAS

The CALIOP, co-developed by NASA and French space agency National Centre for Space Studies, is the primary instrument aboard the polar-orbit, sun-synchronous and part of the Afternoon-Train (A-Train) constellation of satellites, CALIPSO. CALIOP provides unique vertically-resolved measurements of aerosols and clouds on a global scale, since June 2006 (?). To achieve its scientific objective, CALIOP operates a near-nadir viewing two-wavelength (532 nm and 1064 nm) polarization-sensitive (532 nm) elastic backscatter Nd: YAG lidar (Winker et al., 2007). Here we utilize CALIOP Version 4.2 level 2 aerosol and cloud profiles of backscatter coefficient, particulate depolarization ratio, and extinction coefficient at 532 nm, provided in a uniform 5 km horizontal and 60 m vertical resolution along the CALIPSO orbit track, to describe the vertical distribution of the dust event. Moreover, the atmospheric classification products of “Feature Type” and “Aerosol Subtype” are used to present the atmospheric structure and aerosol composition. More specifically, the “Feature Type” algorithm classifies the detected atmospheric features in distinct classes, as “clear air”, “cloud”, “low/no confidence cloud”, “tropospheric aerosol”, “low/no confidence tropospheric aerosol” “surface”, “subsurface” and “totally attenuated”, while recent advances expanded the Feature Type algorithm with the “stratospheric aerosol” class. For the “tropospheric aerosol” related “Feature Type” class (Vaughan et al., 2009), CALIOP Version 4.2 algorithm attempts a further classification of the detected atmospheric features, as “marine”, “dust”, “polluted continental”, “clean continental”, polluted dust”, “elevated smoke” and “dusty marine”. The study implements CALIOP backscatter coefficient and extinction coefficient profiles at 532 nm along the CALIPSO track, complementarily to MIDAS DOD550, towards the full three-dimensional description of the dust event that occurred between May 2 and May 4, 2018. Also, for the needs of the study, the CALIPSO-based pure-dust product developed in the framework of the European Space Agency LIVAS activity is used (Amiridis et al., 2015). The pure-dust product is based on the assumption that the “polluted dust”, “dust,” and “dusty marine” CALIPSO aerosol subtype classes are external aerosol mixtures of dust and non-dust components. Accordingly, based on a depolarization-based methodology (Tesche et al., 2009) developed in the framework of the European Aerosol Research Lidar Network (Pappalardo et al., 2014; Earlinet, 2020) and several quality assurance procedures (Marinou et al., 2017; Tackett et al., 2018) decouples the pure-dust backscatter coefficient component at 532 nm from the total aerosol mixture (Amiridis et al., 2013). Finally, the implementation of a Lidar Ratio suitable for Middle-East dust (Baars et al., 2016; Filioglou et al., 2020), provides the pure-dust extinction coefficient profiles at 532 nm (Proestakis et al., 2018). The quality filters are concerned with the aerosol extinction uncertainty, extinction quality control flag, misclassified cirrus, isolated 80 km layer, large negative near-surface extinction, undetected surface-attached-aerosol low bias, removal of samples below opaque aerosol layers and surface contamination beneath surface-attached opaque layer (Amiridis et al., 2015).

2.1.4. Surface-based data (Aeronet and BSRN)

The Aeronet data used in this work are obtained for the stations of the Indian region located at India Meteorological Department (IMD) New Delhi, Kanpur, and Gandhi College where the measurements are taken with a CIMEL sunphotometer (CE318). The instrumentation and calibration procedure, and data acquisition and retrieval algorithms conform with the Aeronet standards (Dubovik et al., 2000; Holben et al., 2001). The Aeronet ground-based AOD is available at a high temporal resolution of about 1 per 10 min that was used to evaluate the accuracy of the quality assured CAMS AOD and MODIS AOD used in this study. The evaluation analysis has been performed by utilizing the AOD retrieved at 500 nm and further converted to 550 nm for comparison using Ångström (Lozano et al., 1998) law as

$$\frac{\mathrm{AOD}_2}{\mathrm{AOD}_1} = \left(\frac{\lambda_2}{\lambda_1}\right)^{\alpha}, \tag{1}$$

where λ refers to the wavelength at which the AOD is taken, and α refer to the Ångström exponent for the desired wavelength range. In this analysis, λ_1 and λ_2 corresponds to the wavelengths 500 nm and 550 nm, respectively and AOD_1 and AOD_2 refers to the AOD values at 500 nm and 550 nm, respectively. The Ångström exponent is considered corresponding to the wavelength range of 440–675 nm (Lozano et al., 1998). However, the extreme atmospheric conditions result in a reduced amount of inversion outputs to the sun-direct measurements or the Spectral Deconvolution Algorithm (O’Neill et al., 2003) retrievals that lead to an increase in the number of missing data. In order to deal with the data gaps in the Aeronet measurements and get a better visualization of the AOD variation, we have considered the Aeronet version 3 Level 1.0 and Level 1.5 AOD observations and Ångström exponent.

BSRN data is used to obtain the ground measurements of surface irradiance from the station of Gurugram, India (Ramanathan, 2019).

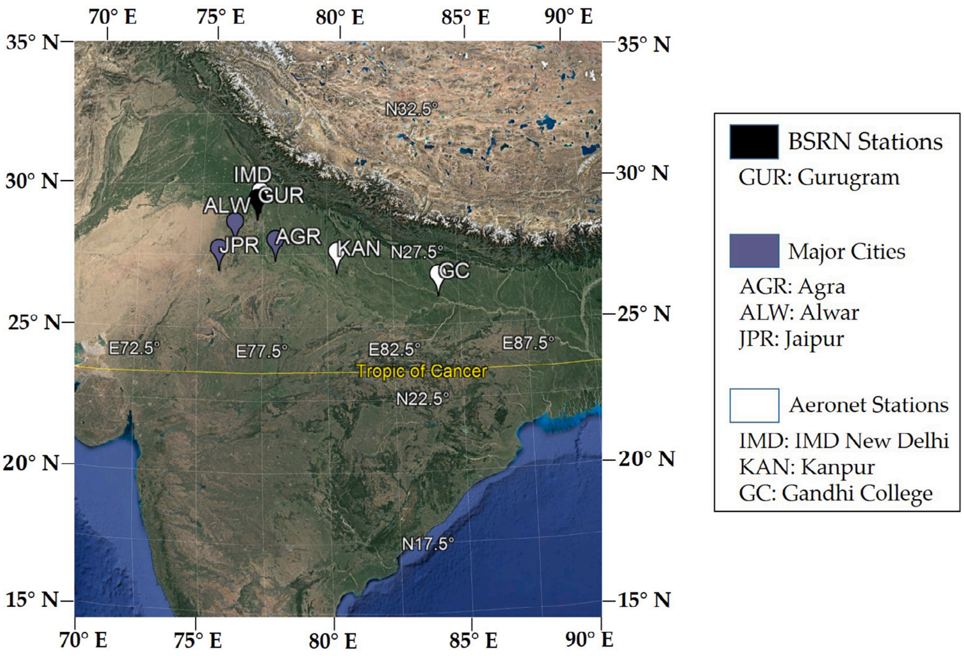

Fig. 1. Map of northern India with Aeronet and BSRN stations and major cities.

The Gurugram BSRN station is located at an altitude of 259 km, a latitude of 28.42° and a longitude of 77.16° as shown in Fig. 1. BSRN stations provide high-precision ground measurements of solar irradiance including shortwave downward global radiation and direct radiation at a temporal resolution of 1 min. The dataset used for the comparison in this study is from May 2 to May 4, 2018. Fig. 1 provides a depiction of all the locations that have been selected for this study, including the BSRN station, Aeronet station, and the major cities affected by the dust storm of 2018.

2.2. Methodology

Fig. 2 shows the layout of the methodology followed for the analysis of the dust event and solar energy forecasting. In order to capture the dust event, the MIDAS dataset was used to exploit its AOD and DOD. After obtaining the dust peak, CALIPSO profiling was used to analyze the vertical structure and components of the aerosol during the dust event. This was followed by the solar irradiance forecasting using the WRF model and the CAMS AOD for the dust case.

2.2.1. WRF and dust assimilation techniques

The dust event was analyzed using the WRF model (Skamarock et al., 2008) which is a mesoscale NWP model that is provided by the National Center for Atmospheric Research. In this study, WRF Version 4.0 was configured as shown in Table 1 with the boundary conditions derived from the GFS model at a spatial resolution of 27 km with initialization at 00 UTC. The domain is divided into 33 vertical terrain-following levels to facilitate low-altitude marine layer stratocumulus formation. The microphysics was dealt with using the New Thompson scheme with cumulus parameterization using the Tiedtke scheme and shortwave and longwave radiation with the Rapid Radiative Transfer Model (RRTM). The New Thompson package is a bulk microphysics scheme used for cloud microphysics parameterization (Thompson et al., 2008). An explicit prediction of the interaction between six classes of water (rain, snow, graupel, cloud ice, water vapor, and cloud water), in addition to the cloud ice, rain number concentration is carried out by the Thompson model, which is a hybrid double moment ice and rain parameterization. Tiedtke cumulus parameterization (Tiedtke, 1989) is applied for sub-grid scale vertical mixing which is a mass-flux scheme that deals with the parameterization of shallow, deep, and midlevel convection. This scheme considers entrainment, detrainment, and downdrafts to represent the cloud ensemble by a bulk cloud model. An 80% minimum relative humidity is imposed for the mean value between the cloud top and base to limit the deep convection in drier regions. The parameterization of the planetary boundary layer mixing is carried out using the Mellor–Yamada–Janjic scheme (Janjic, 1990) that represents a non-singular implementation of the turbulence closure model of Mellor–Yamada level 2.5 (Mellor and Yamada, 1982).

The irradiance is calculated using the RRTMG shortwave scheme (Iacono et al., 2008) that accounts for clear-sky scattering, cloud absorption, cloud reflection, and water vapor absorption. To take into account the significant downward flux originating from above the model top, the longwave scheme has been modified at the top-of-atmosphere (Cavallo et al., 2010). RRTM is a widely used state-of-the-art radiative transfer model for applications related to climate and weather in which spectral bands and the k-distribution method of integration with look-up tables are used for efficiency. For the vertical variation of clouds, Monte Carlo Independent Column Approximation is used along with a maximum-random overlap assumption by default. It takes into account the effect of ozone through a global monthly climatology option that comes from the CAM3 data, and trace gases are also included along with their time variation for climate projections. Aerosols are included in the model using global monthly climatology or can be specified/input in other ways. In this work, for the basic WRF runs, the aerosol data is included in the simulations based on Tegen climatology (Tegen et al., 1997), which takes into account organic carbon, black carbon, dust, stratospheric aerosol, sulfate, and sea salt.

Table 1
WRF model configuration.

Characteristic	Model configuration
Simulation period	2nd to 4th May 2018
Domain	Northern India
Initialization	NCEP GFS data at 00 UTC
Forecast interval	Hourly
Microphysics	New Thompson scheme
Shortwave Radiation scheme	Rapid radiative transfer model
Planetary boundary layer	Mellor–Yamada–Janjic
Cumulus parameterization	Tiedtke scheme

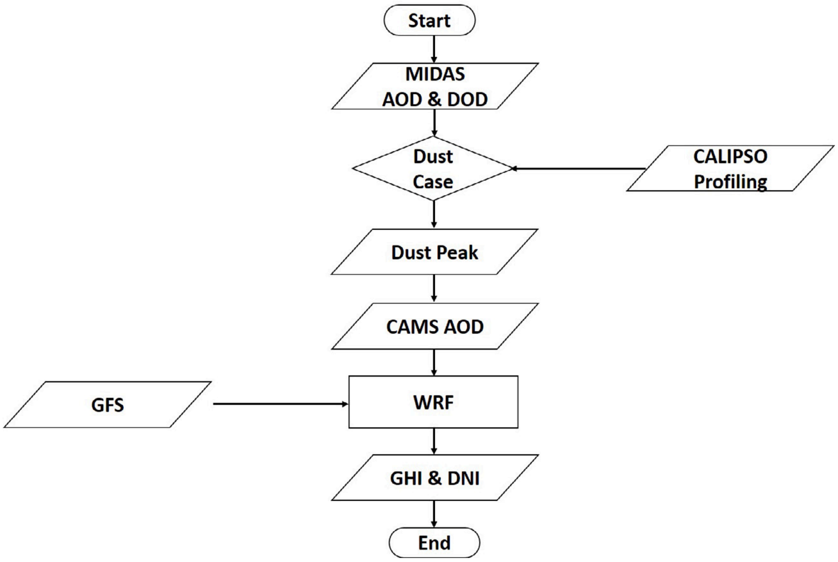

Fig. 2. Flowchart of the dust case analysis and solar energy forecasting.

Table 2
WRF model configuration.

Characteristic	Model configuration
Simulation period	2nd to 4th May 2018
Input	Solar zenith angle Aerosol optical depth (CAMS, Aeronet, MODIS)
Output	Hourly

The data has spatial variations as 4 in latitudes and 5 in longitude and monthly temporal variation. CAMS AOD at 550 nm is included in the WRF model using the aerosol input options for the RRTMG scheme, but the aerosols are constant during the model integration (Wang et al., 2019).

2.2.2. INSIOS simulations

The INSIOS is an analytical radiative transfer model based technique used for the estimation of solar irradiance and was developed for the application to the Indian climatological conditions. It is based on the Solar Energy Nowcasting SystEm (Kosmopoulos et al., 2018b). The model utilizes the radiative transfer model (Libradtran) simulated GHI and DNI which is based on CAMS AOD as input that was used to train the multi-polynomial regression function for the clear-sky condition. In this work, the GHI and DNI are obtained using the INSIOS model for clear-sky according to the work presented in Masoom et al. (2020a) as

$$\begin{aligned} f(x,y) = {} & p_{00} + p_{10}x + p_{01}y + p_{20}x^2 + p_{11}xy + p_{02}y^2 + p_{30}x^3 + p_{21}x^2y \\ & + p_{12}xy^2 + p_{03}y^2 + p_{40}x^4 + p_{31}x^3y + p_{22}x^2y^2 + p_{13}xy^3 + p_{04}y^4 \\ & + p_{50}x^5 + p_{41}x^4y + p_{32}x^3y^2 + p_{23}x^2y^3 + p_{14}xy^4 + p_{05}y^5 + p_{60}x^6 \\ & + p_{51}x^5y + p_{42}x^4y^2 + p_{33}x^3y^3 + p_{24}x^2y^4 + p_{15}xy^5 + p_{06}y^6 \end{aligned} \tag{2}$$

where x is the solar zenith angle, and y is AOD for clear-sky condition. The coefficients of Eq. (2) are taken from the work presented in Masoom et al. (2020a). INSIOS simulation details are provided in Table 2.

3. Results

3.1. Observations (MIDAS, CALIPSO, CAMS, Aeronet)

Fig. 3 shows the total AOD and total DOD as obtained from the MIDAS dataset. May 3 and 06 UTC were chosen for simulations as this was the best time step to capture the effects as the dust event was at the peak and to a great extent to the whole region. The MIDAS had the largest values for the specific locations in the Northwestern part of India. We can see that the total AOD is varying from 1 to 1.5 in the Northwestern region of India with few areas having AOD up to 2, mainly covering the Rajasthan region. This high amount of AOD is the effect of the dust storm of May 3 that entered India through the northwestern front. The total DOD in the same region is found to vary from 1 to 1.5 which indicates a significant fraction of dust in the total AOD.

The dust transportation mechanisms associated with the transport of dust over the Indian subcontinent are discussed here. The air masses travel over a long distance from their origin transporting the dust aerosols during the dust storm (Huang et al., 2015). The East Asian deserts produce a large amount of mineral dust particles that become entrained in the atmosphere and are transported to the Indian region during the summer (Huang et al., 2007). An upper-level jet stream, an upper trough and the subtropical high jointly led to the eruption of the dust storm from the Thar Desert (TD) (Wang et al., 2020b). The atmospheric circulation conditions and local topographical constraints led to the accumulation of the dust storm over the Himalayan foothills that further traveled eastward and southward and affected the entire Indian-Gangetic Plain. A stronger upward movement and the interaction between several macro-scale weather systems circulation led to the upliftment and transport of dust aerosols from TD across the majestic Himalayas to the IGP. A synergy of the subtropical high, the northwest cold air and higher temperature anomaly induced the eruption of this dust storm from the Thar desert and as a consequence of their joint effects, the spatial coverage of the dust storm was extended across the IGP. The connection between the dust aerosol from the TD and stronger secondary circulation upward movement led to a much stronger and higher vertical uplift of the dust aerosols over South Asia that transported the dust aerosols over South Asia up to the Himalayas (Jin et al., 2015). A similar dust event was presented in Chen et al. (2017) in which authors reported that the northwest flow along the mountain region, that accumulated a mass of cold air, was then injected into the desert and the creation of a low-level convergence, due to the merging of warm and cold air, build the dynamic conditions for dust emission from the desert area.

Dust-induced atmospheric heating leads to a low-pressure system which creates a convergence region where the strengthened southwesterly winds transport more water vapor from the center, which lies in the Arabian sea, northeastward to the Indian subcontinent (Jin et al.,

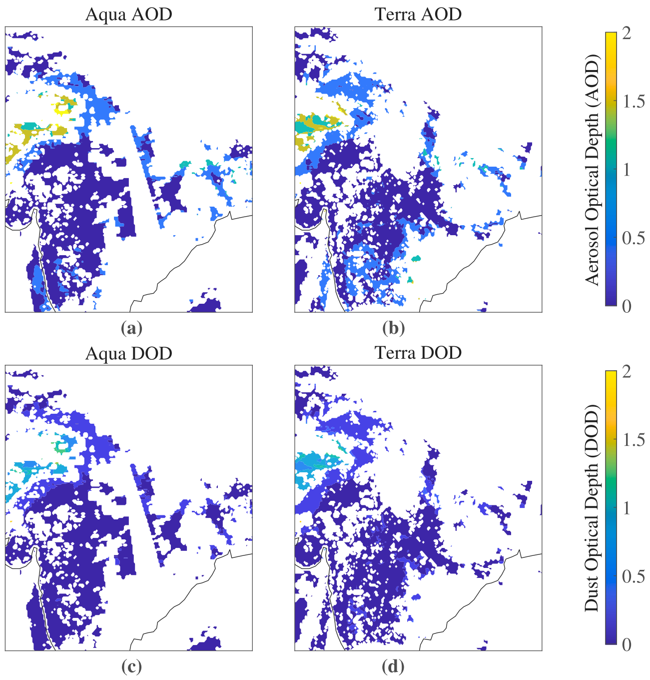

Fig. 3. MIDAS dust optical depth map for May 3, 2018.

2015). The south–north thermal contrast in the mid-upper troposphere is more important for the Asian monsoon than that in the lower troposphere. A positive feedback is formed by more dust emission due to the strengthened northwesterly winds over the Arabian Peninsula and transportation to the Arabian sea. The strong “Shamal” winds in Arabian Peninsula and Iberian Peninsula lead to the development of frequent dust storms in the boreal summer whose long-distance transport goes to the Arabian sea and further to the Indian subcontinent. Dust aerosols are one of the important light-absorbing impurities which are closely related to human activities, dust sources and biomass burning (Wang et al., 2020b). The dust aerosols accumulated in the Thar desert can be lifted up migrating into the IGP. Furthermore, dust particles in Northeastern Africa and the Middle East are also transported eastward following the westerly jet and then transported into the IGP through the western part of the Indian subcontinent.

CALIPSO nighttime observations on May 3, 2018, are used to depict synergistically with MIDAS the horizontal and vertical structure of the dust event over the Indian subcontinent. Fig. 4a shows the CALIPSO-India overpass, the “Aerosol Subtype” product (Fig. 4b), and also the total backscatter coefficient and total extinction coefficient profiles at 532 (Fig. 4c and 4d). Fig. 4e and Fig. 4f present the quality assured pure-dust backscatter and extinction coefficients at 532 nm whose details are provided in Section 2.1.3. Based on CALIPSO aerosol subtype classification, it is apparent that dust and polluted dust aerosol types are mainly present during the event over the Indian peninsula. Hence, we have used DOD only to analyze the event and the simulations are purely based on AOD. The CALIPSO observations are only used for analysis as it is not reliable for RTM simulations because of the contamination of signals near the surface and below 2 km of height (Tackett et al., 2018). However, CALIPSO is useful in order to see the vertical distribution of the dust layer and its extent. The vertical distribution of dust plumes is an important factor to be considered for the assessment of dust radiative forcing.

Fig. 5 shows the variation of BSRN GHI and DNI and Aeronet AOD during the time period of three days covering the dust storm from May 2 to May 4. The BSRN GHI and DNI are shown for the station of IMD New Delhi while the Aeronet AOD is shown for the stations of Delhi, Gandhi College, and Kanpur. The BSRN GHI and DNI for 3 days (before, during, and after the dust event) and the Aeronet AOD are shown to see the direct aerosol effect on the solar irradiance. It is observed that there is a lot more fluctuation in GHI as well as DNI on May 3 around 6 UTC than the other two days indicating the peak of the dust storm. During this time, the unavailability of the Aeronet AOD has to do with the cloud flagging of the Cimel algorithm.

3.2. WRF simulations

Fig. 6 shows the variation of GHI and DNI as obtained from the WRF simulation basic run, and the assimilated CAMS run for the extreme dust event of May 3, 2018. It is seen that the dust event is captured more accurately in WRF-CAMS runs, which can be attributed to the finer resolution of the CAMS AOD forecasts. There is a significant reduction in GHI and DNI due to the direct impact of the dust storm on solar irradiance.

The dust aerosols tend to heat the atmosphere by absorbing the solar radiation with a more effective absorption over bright surfaces as the radiation undergoes multiple reflections between the dust layers and bright land surfaces (Jin et al., 2015). The fine dust particles tend to absorb the solar radiation 3 to 5 times as compared to the coarse particles. Due to the blocking effect of dust, less LW radiation is absorbed by the atmosphere above the dust layer, which results in an atmospheric cooling effect. However, a positive forcing is observed in the northern Indian Ocean and the Bay of Bengal. At the surface, dust aerosols block SW radiation from reaching the surface through scattering and absorption resulting in a surface cooling effect, however, it results in warming effect over the Indian subcontinent. The dust aerosol induced positive SW radiative forcing led to warming because of dust absorption. The radiative heating rate is maximum where the dust mass loading is greatest and gradually decreases with height (Chen et al., 2017). East Asian dust during the dust storm event plays a major role in the radiation budget. The atmospheric absorbing aerosols influence the net radiation between atmosphere and surface by absorbing and scattering solar radiation as well as interacts with terrestrial long-wave radiation. Absorbing aerosols also contribute to large diabatic heating in the atmosphere, enhancing cloud evaporation. Besides, the absorbing aerosols also influence the cloud properties and climate by acting as cloud condensation nuclei and ice nuclei. An increase in moisture, cloudiness and deep convection over northern India is seen due to the aerosol direct forcing on the atmosphere–land system as the dust aerosol produces atmospheric dynamical feedback by heating mid-troposphere (Wang et al., 2020a). The strong light-absorbing atmospheric particles alter the radiation balance by direct, indirect and semi-direct effects.

Fig. 7 presents the WRF simulations with CAMS AOD ingestion and a direct comparison between the simulations obtained from the ingestion of AOD from MODIS observations and CAMS forecasts. Fig. 7a shows the observed AOD distribution as obtained from MODIS level 3 and simulated/forecasted CAMS MACC AOD at 550 nm. From CAMS AOD contours, it is clear that the dust peak is over Northwest India, mainly covering the Rajasthan region on May 3 at 06 UTC. Hence, the MODIS AOD was also considered for the same period to see how well the model monitors the dust case sequence and to see the model vs observation differences from the WRF model. The spatial distribution of the model AOD values (at 550 nm, 06 UTC) was observed to be in good match with the satellite (MODIS) retrievals. The CAMS forecasts follow the dust plume pattern as observed by MODIS but underestimate the peak AOD values which can be due to higher model spatial resolution of 0.25° as compared to the satellite data (1°).

The underestimation of aerosol direct radiative forcing as observed from the distribution is a result of the imperfection of the forecasted meteorology and the diming of the MODIS AOD initial assimilation impact (Allen et al., 2013; Basart et al., 2019). However, even though

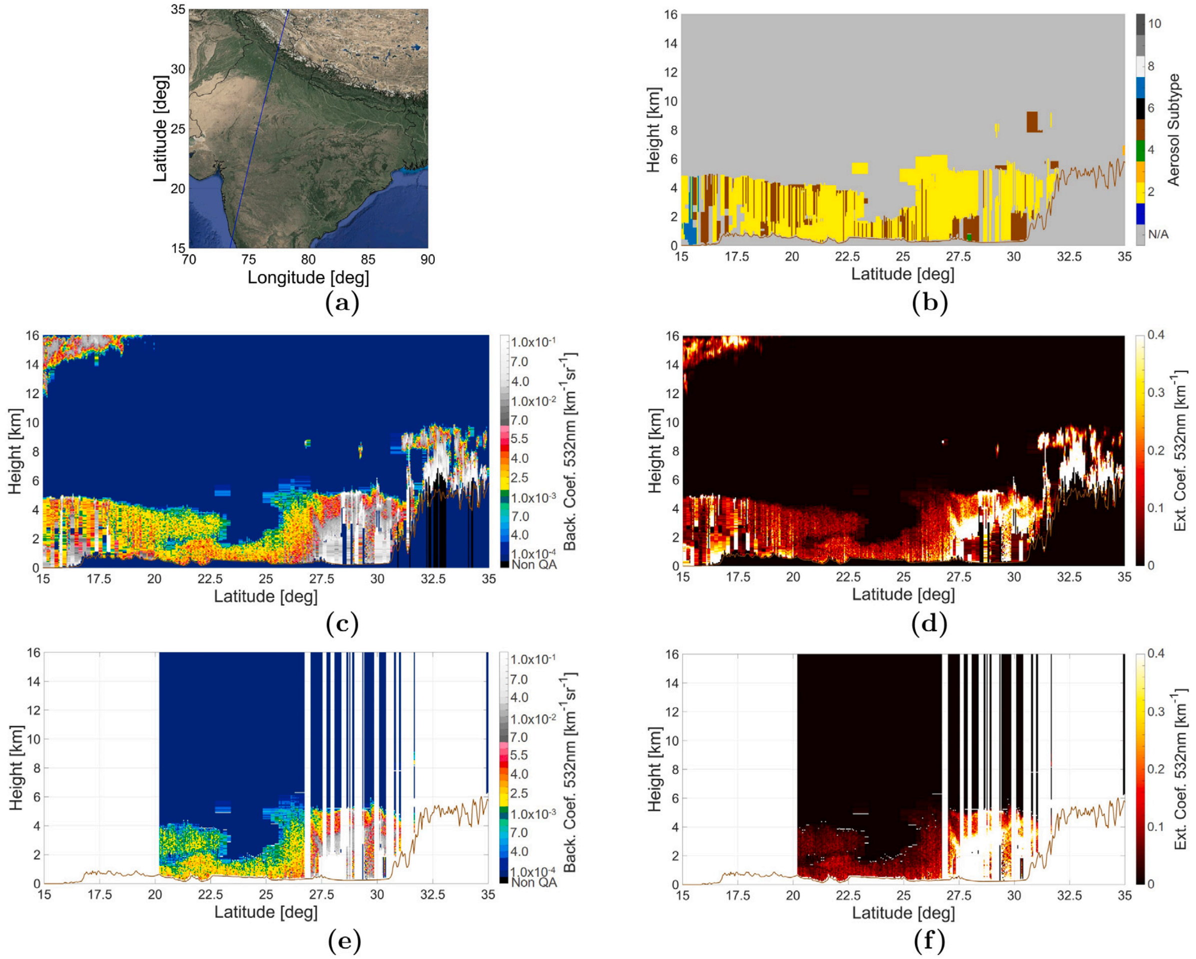

Fig. 4. CALIPSO-CALIOP profiling of the dust incursion over the India subcontinent on May 3, 2018: (a) CALIPSO nighttime orbit, (b) “Aerosol Subtype” classification, (c) total backscatter coefficient at 532 nm, (d) total extinction coefficient profile at 532, (e) the corresponding quality-assured pure-dust backscatter coefficient at 532 nm, and (f) pure-dust extinction coefficient at 532 nm.

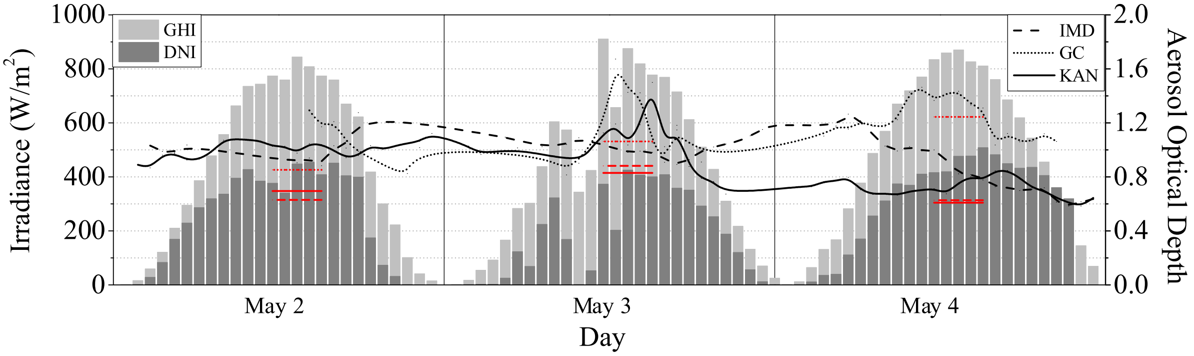

Fig. 5. Aeronet AOD and BSRN GHI and DNI for the dust storm of May 2018. The red inserts represent the MODIS AOD. (For interpretation of the references to color in this figure legend, the reader is referred to the web version of this article.)

there are differences in AOD, the impact on the irradiance simulations is of the order of 1% in most cases (> 80% of the spatial coverage). This highlights the fact that CAMS MACC forecasts are an important and useful tool in solar energy potential estimation, planning, and policy-making (Kosmopoulos et al., 2015; Langerock et al., 2015; Charabi and Gastli, 2012). There is a plume patch in this region as can be seen from Fig. 7a of CAMS AOD which lead to the decrease in GHI as can be seen from Fig. 7b base case run without aerosol (WRF0), WRF-CAMS, and WRF-MODIS. The reduction in the DNI is more pronounced for these cases.

Fig. 7b shows the aerosol-free, CAMS-based, and MODIS-based GHI and DNI simulations near the local-noon. The AOD retrieval corresponds to 550 nm having a spatial resolution of 0.4 × 0.4 degrees for CAMS and 1 × 1 degrees for MODIS. The CAMS simulation has a temporal resolution of 1 per hour, and 1 per day for MODIS, which spots the ability of CAMS in providing conclusive information on the evolution of the availability of solar energy temporally. Fig. 7c characterizes the impact of dust on solar irradiance as GHI and DNI percentage attenuation, which is indicative of the dust plume radiative impact over India. The smoothing technique was applied in Fig. 7c

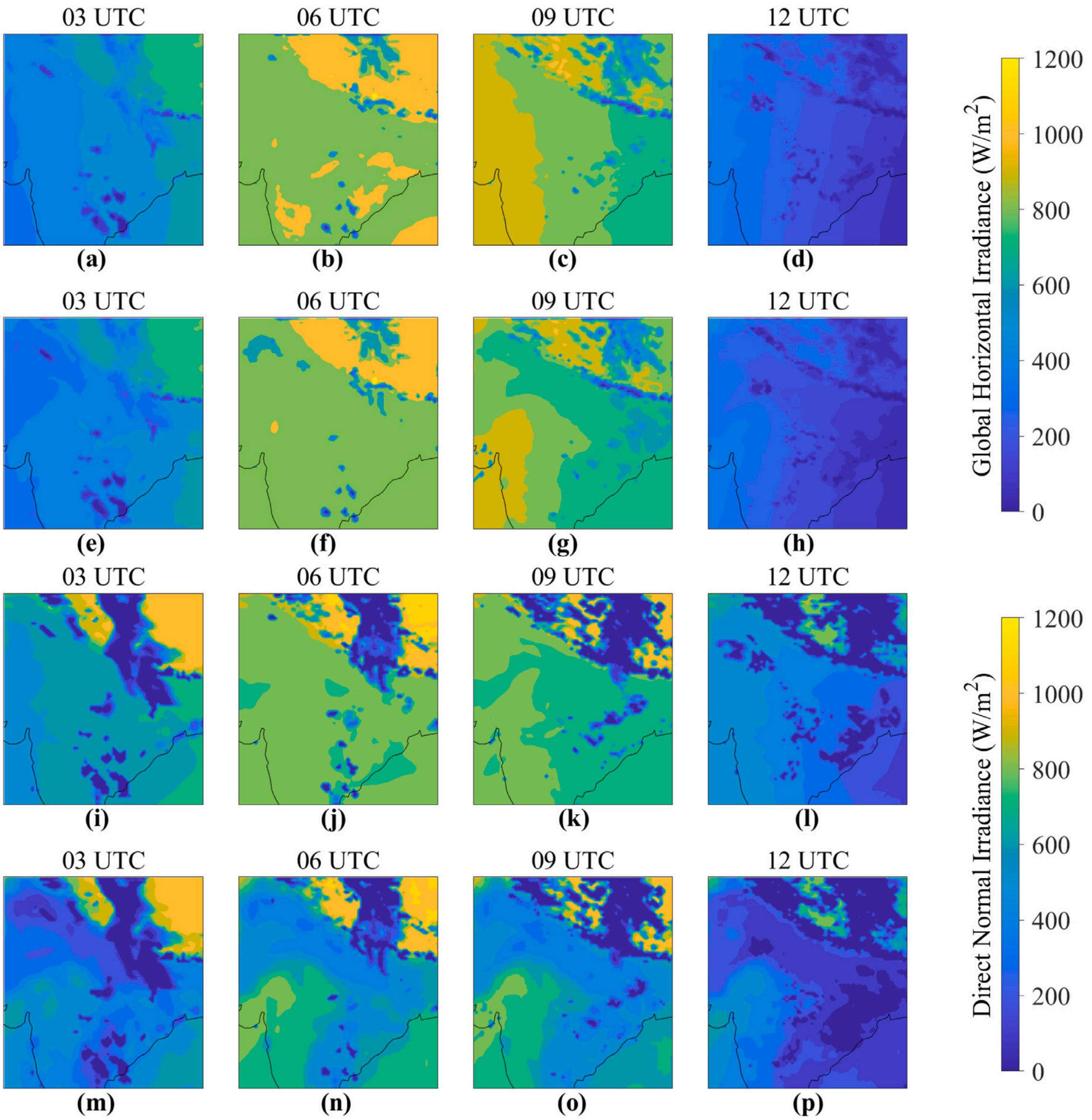

Fig. 6. WRF plain runs vs. assimilated CAMS runs of GHI (a–h) and DNI (i–p) at 03 UTC, 06 UTC, 09 UTC and 12 UTC for extreme dust event of May 3, 2018.

to fit the contour lines for better visualization of results. The mean GHI values from simulated results were found to be about 1006 W/m^2 under aerosol-free conditions, while it reduced to about 930 W/m^2 with CAMS AOD and 950 W/m^2 with MODIS AOD for full aerosol conditions. The corresponding radiation values of DNI are 889 W/m^2 for clear sky and around 614 W/m^2 and 694 W/m^2 for dust event conditions with CAMS and MODIS AOD, respectively. The integrated WRF and CAMS simulations show that the differences are significant for DNI for the aerosol input data source from CAMS, while only a few regions show the extra information of CAMS ingestion since the effect on GHI is smaller. The average percentage impact of the dust (Fig. 7c) in the northwestern region is found to be around 9% and 11% for GHI and 33% and 41% for DNI for MODIS and CAMS, respectively. Hence, it is highlighted that there is a much more enhanced attenuation of solar irradiance's direct component and provides a convincing conclusion regarding the energy losses to concentrating solar power applications.

3.3. INSIOS simulations (CAMS vs Aeronet)

We have performed the analytical radiative transfer model simulations for irradiance estimations to analyze the event. Fig. 8 shows the variation of GHI and DNI for three days timelapse as simulated through the analytical model INSIOS with Aeronet AOD, CAMS AOD and MODIS AOD, and comparison with the respective measurements of BSRN Delhi station to see how close to reality the simulations are able to reach. It is observed that there is a significant reduction in GHI and DNI as measured by the BSRN Delhi station on May 3 around 06 UTC when the dust storm was at its peak. In the case of GHI, it is seen that the INSIOS simulations are following an almost similar patterns with Aeronet, CAMS and MODIS inputs and are able to match the BSRN pattern with some deviations. In the case of DNI, there are a lot more fluctuation in the patterns obtained from Aeronet, CAMS and MODIS inputs as compared to the BSRN measurements for all days. However, INSIOS with CAMS AOD input is able to better capture the dust event of May 3.

Fig. 9 shows the scatter plots of CAMS and Aeronet AOD and the INSIOS simulations using CAMS and Aeronet AOD for the estimation of GHI and DNI for a period of three days covering the dust event excluding the early morning and the late-night data comparisons. The correlation coefficient between Aeronet and CAMS AOD was found to be as 0.65. In Eskes et al. (2015), the authors found a correlation between the Aeronet and CAMS dataset to be in the range of 0.65 to 0.8.

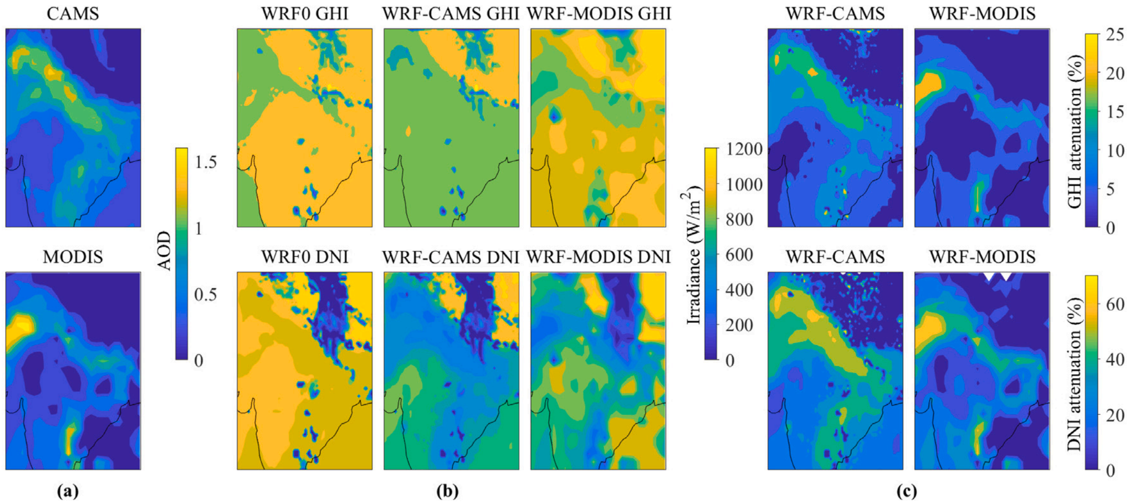

Fig. 7. (a) AOD from MODIS and the CAMS 1 day ahead forecast. (b) WRF simulations at local noon on the day of the peak of the dust event on May 3, 2018 for GHI and DNI. GHI0 and DNI0 represent the simulations without aerosols (with only the effects of SZA). (c) The percentage attenuation relative to the aerosol-free simulations for GHI and DNI under MODIS- and CAMS-based AODs.

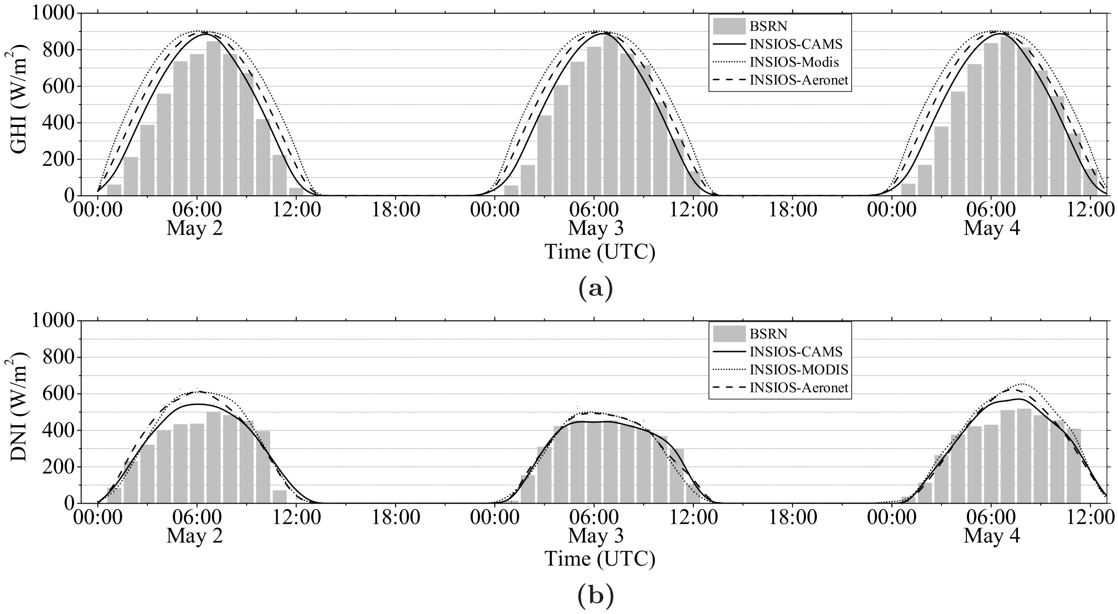

Fig. 8. INSIOS simulations of (a) GHI and (b) DNI with Aeronet and CAMS inputs vs BSRN Delhi 3 days timelapse.

Similar correlations were also observed in other studies including (Kosmopoulos et al., 2018a; Perez et al., 2013; Kosmopoulos et al., 2018a; Masoom et al., 2020a). There are overestimations from MACC modeling as compared to the Aeronet data for most of the cases. Fig. 9b and 9c show the scatterplot between GHI and DNI, respectively, as obtained by using CAMS AOD and Aeronet AOD. The correlation between INSIOS-CAMS GHI and INSIOS-Aeronet GHI was found to be around 0.98 and in the case of DNI it was observed to be 0.98. Hence, it is interpreted that the AOD differences observed between CAMS and Aeronet minutely affect the GHI and DNI estimations. This data behavior shows that AOD absolute differences, with relative root mean square error of about 10.68%, led to an absolute difference in solar radiation less than 2% for daytime irradiances (relative RMSE is 8.19% and 8.31% for GHI and DNI, respectively) as presented by authors in the various similar comparison approaches (Eskes et al., 2015; Kosmopoulos et al., 2017a, 2018a; Akritidis et al., 2017; Schroedter-Homscheidt et al., 2013).

3.4. Simulations vs reality (WRF and INSIOS vs BSRN, SODA, and INSAT)

SOlar radiation DAtabase (SODA) irradiance data is retrieved from the McClear clear-sky irradiation service provided by CAMS which provides time series irradiance data of the entire globe under cloud-free conditions (Gschwind et al., 2019). Indian National Satellite System (INSAT) irradiance was retrieved from mosdac (Mosdac, 2020) which is based on a spectral irradiance model (Paulescu and Schlett, 2003) and provides half-hourly irradiance data (ISRO, 2015).

Fig. 10 shows the variation in GHI and DNI for Delhi, Agra, Jaipur, and Alwar as obtained from BSRN measurements and WRF, SODA, INSAT, and INSIOS models. A good correlation can be seen in the case of GHI from all the models for all the stations with small deviations in the case of INSAT GHI for Agra and Jaipur. The deviation is observed around the solar noon which might be due to the fact that the dust event is not captured well by this model and leads to erroneous radiance data to satellite which in turn affects the GHI estimation.

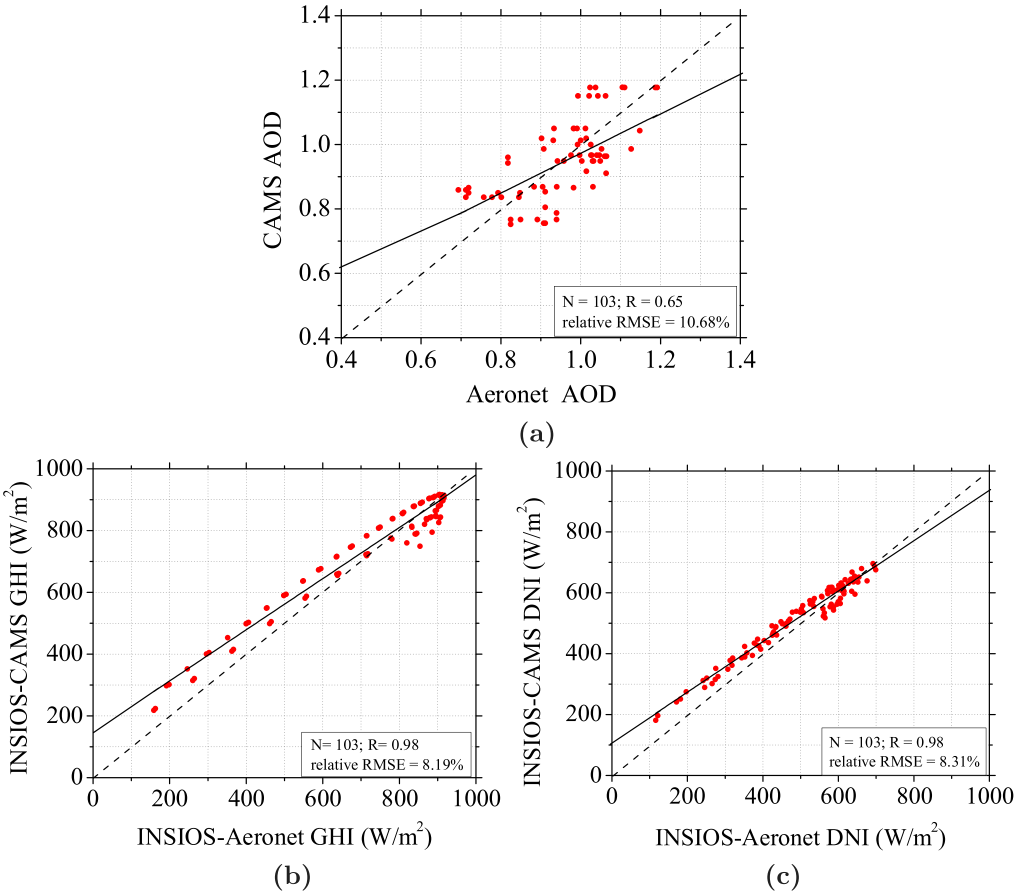

(a)

(b)

(c)

Fig. 9. Scatter plots of CAMS and Aeronet AOD (a) and INSIOS-CAMS vs INSIOS-Aeronet (b) GHI and (c) DNI, respectively, for the three days May 2–May 4, 2018. The relative RMSE is calculated with reference to the Aeronet data.

From Fig. 10a, it is seen that all the models are following the BSRN pattern and the models are slightly overestimating the irradiance and the deviation is seen to be maximum in the case of the INSAT model. A much more deviation between the models is seen in the case of DNI. From Fig. 10e, it is observed that WRF and INSIOS models best captures the dust event as they are seen to closely follow the BSRN pattern as compared to SODA and INSAT models. INSAT model turns out to be the worst-performing model as it is based on satellite radiance which might have caused due to erroneous satellite observations during the dust event. The variation of the models in comparison to BSRN measurements is discussed in detail in Fig. 11 that shows the GHI and DNI percentage difference between the BSRN measurements and the corresponding irradiance obtained from WRF, SODA, INSAT, and INSIOS models. It is seen from Fig. 11a that almost all the models tend to overestimate GHI with a bit of underestimation from WRF and SODA models for few time steps. Moreover, the SODA model is seen to estimate GHI almost within a deviation of 20 W/m^2 from BSRN measurements. However, the GHI percentage error is varying from −20% to 10% for all the models in the case of GHI, and higher errors are observed during early morning and late evening hours. While in the case of DNI, both underestimations and overestimations are seen from all the models. WRF and SODA models mostly underestimate DNI while INSIOS and INSAT models overestimate DNI. WRF seems to be the best performing model having the deviation from BSRN measurements almost within 50 W/m^2. WRF and INSIOS models are showing variations within ±20%, while the SODA model is showing underestimations and INSAT models are seen to mostly overestimate DNI.

4. Discussion

4.1. Impact of dust on surface solar irradiance

Fig. 12a illustrates the event as provided by the CAMS model forecast. The AOD values are shown for the Indian subcontinent having higher values (AOD = 1.6) in the northern region. The dust source functions have inbuilt uncertainties within the aerosol models that are accounted for by model tuning in comparison to observations (Vogel et al., 2006) which is beyond the scope of the current analysis. The incoming solar irradiance is examined with global and direct components (GHI and DNI), and an analysis was made for their response to the dust plume during the daytime period when the AOD was at its maximum value of around 1.6. The spatial pattern of the reduction in the solar radiation reaching the surface is in resemblance to that of the dust plume. This is due to the atmospheric dust particles being responsible for the absorption and scattering of the incoming solar radiation. A more noticeable decrease reaching up to 600 W/m^2 was observed in the DNI values. The effect on GHI ranges between 250 W/m^2 (at dust core) and 50 W/m^2 (on dust edges) which signifies that the availability of solar energy for exploitation in these areas (Rajasthan and Western Uttar Pradesh) is tremendously affected during the dust storm. The effect on DNI is severe, reaching up to 600 W/m^2 decrease in the irradiance at the dust core and 500 W/m^2 at the dust edges in northern India.

The Himalayan region in the Northeastern part of the domain surprisingly receives an increased amount of GHI and DNI (Fig. 12b and 12c, respectively) during the dust event. This increase may be attributed to the positive feedback of the interaction of dust particles with the atmosphere on solar radiation in areas north of the plume,

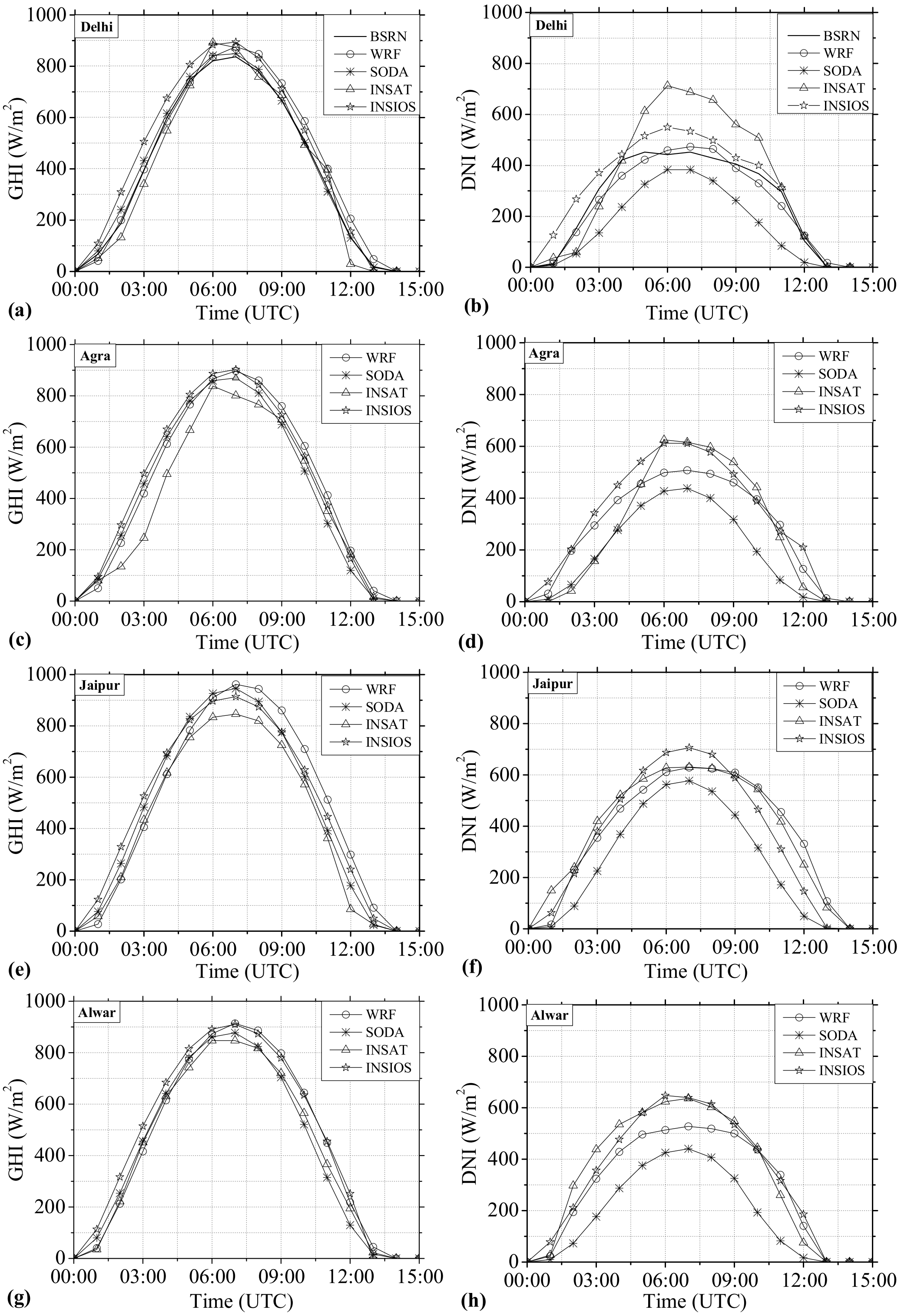

Fig. 10. Diurnal variation of GHI and DNI for Delhi (a, b), Agra (c, d), Jaipur (e, f) and Alwar (g, h) as obtained from BSRN measurements and WRF, SODA, INSAT and INSIOS models on May 3, 2018.

whose significance on solar energy availability is important. Over most of these positively-affected areas, the increase in the GHI is found to be up to 200 W/m^2 and that in DNI up to 400 W/m^2. It seems to follow the mechanism of thermal gradient creation as a consequence of the dust radiative effect, as discussed by the authors in Kosmopoulos et al. (2017b) and Stanelle et al. (2010). Fig. 13 shows the diurnal variation of GHI and DNI obtained from WRF-CAMS and WRF runs with no aerosol interaction for the region divided into four domains based on four geographical directions. The negative impact on solar irradiance due to the dust event is seen from 03 to 12 UTC on May 3, 2018, which maximizes at 07 UTC. The impact is more enhanced for the northwestern domain (Fig. 13a), where the maximum reduction in GHI and DNI are up to around 100 W/m^2 and 400 W/m^2 that corresponds to about 10% and 40% losses of GHI and DNI, respectively. For the remaining domains, the impact on GHI and DNI are limited to 80 W/m^2 (8%) and 300 W/m^2 (33%), respectively.

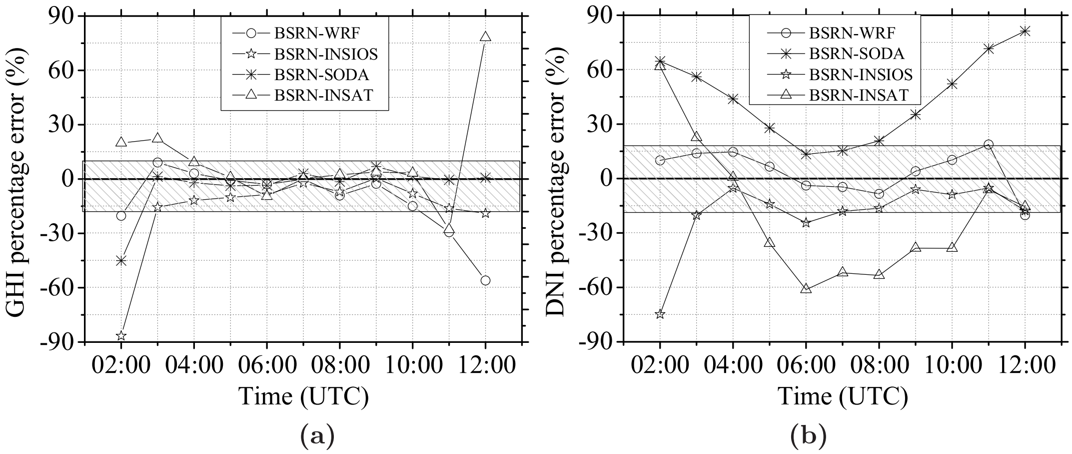

Fig. 11. GHI (a) and DNI (b) difference between the BSRN measurements and the irradiance obtained from WRF, SODA, INSAT and INSIOS models for station Delhi.

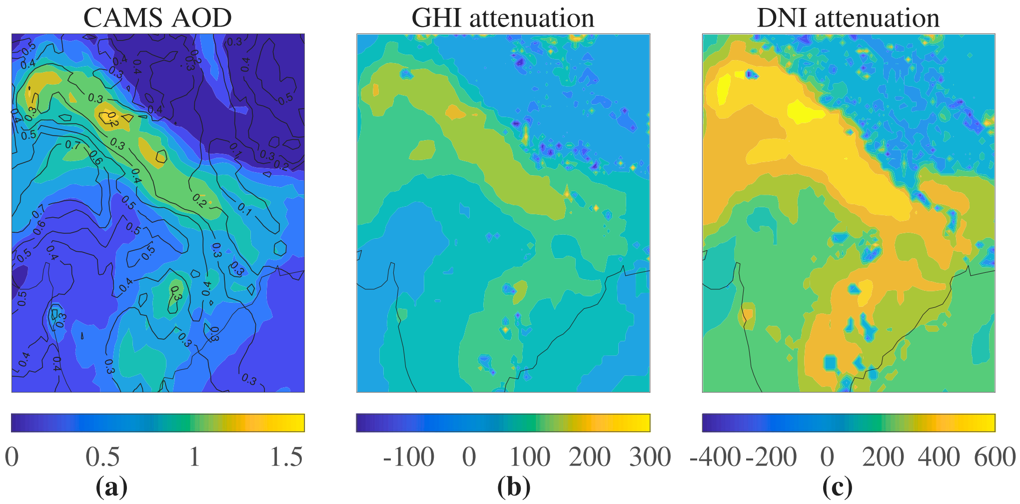

Fig. 12. Spatial distribution of (a) CAMS total AOD (at 550 nm) to 06 UTC. Iso-lines indicate the dust fraction of the total AOD model values. (b) dust plume effect on GHI and (c) DNI (in W/m^2) at surfaces of the extreme dust event of 3 May, 2018 over Northern India as predicted by WRF.

For the investigation of the dust case intensity, a comparison was made between the attenuation in solar irradiance with the variation of AOD over New Delhi (IMD Delhi Aeronet site). It was observed from the AOD values based on the 3 days Aeronet AOD variation (May 2 to May 4, 2018), as shown in Fig. 14 that the range of the AOD values is between 0.85–1.45, with two peaks on May 2 and May 3 at around 18 UTC. May 3 was the peak time of the dust event of 2018 as discussed in Section 1. The dust case selected in this study i.e., on May 3 at 06 UTC lies between these two peaks (May 2 ~ 1.35 and May 3 ~ 1.45). This demonstrates that these two days dealt with the most extreme aerosol events which is mainly due to the intense dust haul on May 3 (with AOD = 1.05 to 1.15 and median value 1.06). The AOD for this period was incorporated into the WRF simulations, and the GHI and DNI percentage attenuation was calculated for 03, 06, 12, and 15 UTC, which are the typical time range for the availability of solar radiation in the Indian region. The results show significantly higher attenuation values around local solar noon (which is around 07 UTC) ranging from 15% and 55% for GHI and DNI, respectively to 28% and 74%, in morning hours and corresponding values of 34% and 81% in the evening hours.

5. Conclusions

This study analyzed and quantified the impact of an extreme dust event on solar irradiance. The usefulness of forecasting dust impact on solar irradiance has a major application to the emerging sector dealing with solar energy exploitation. It includes understanding and determining the range of the dust impact on solar energy attenuation and providing a timely and adequately accurate forecast. In this analysis, the extreme dust event was identified using the earth observation data and its effect on solar irradiance was analyzed from WRF and INSIOS models with CAMS AOD forecast as input. CAMS AOD inputs were evaluated with MIDAS and Aeronet data and also the effect of their differences on solar radiation was made through the INSIOS and WRF models and the validation was done using BSRN ground-based data. INSAT, SODA ad BSRN data were used for solar radiation comparisons with the WRF and INSIOS simulations. The effect of dust on solar radiation was presented with both measurements and forecasting models.

The analysis of the dust event of May 3, 2018 was initiated by mapping and studying its structure via the synergy of MIDAS and CALIOP/CALIPSO space-borne observations along with CAMS MACC forecasts. Variation in the AOD at 550 nm was found to be from 0 to 1.5 in the northwestern domain of India, mainly covering the Rajasthan region, which was the effect of the dust storm of May 3, 2018. The CAMS AOD forecasts followed the dust plume pattern as observed by MODIS, matching with its distribution but with a slight underestimation in the peak AOD values (CAMS ≈ 1.4 max and MODIS values ≈ 1.6 over the Indian region). Even though there are differences

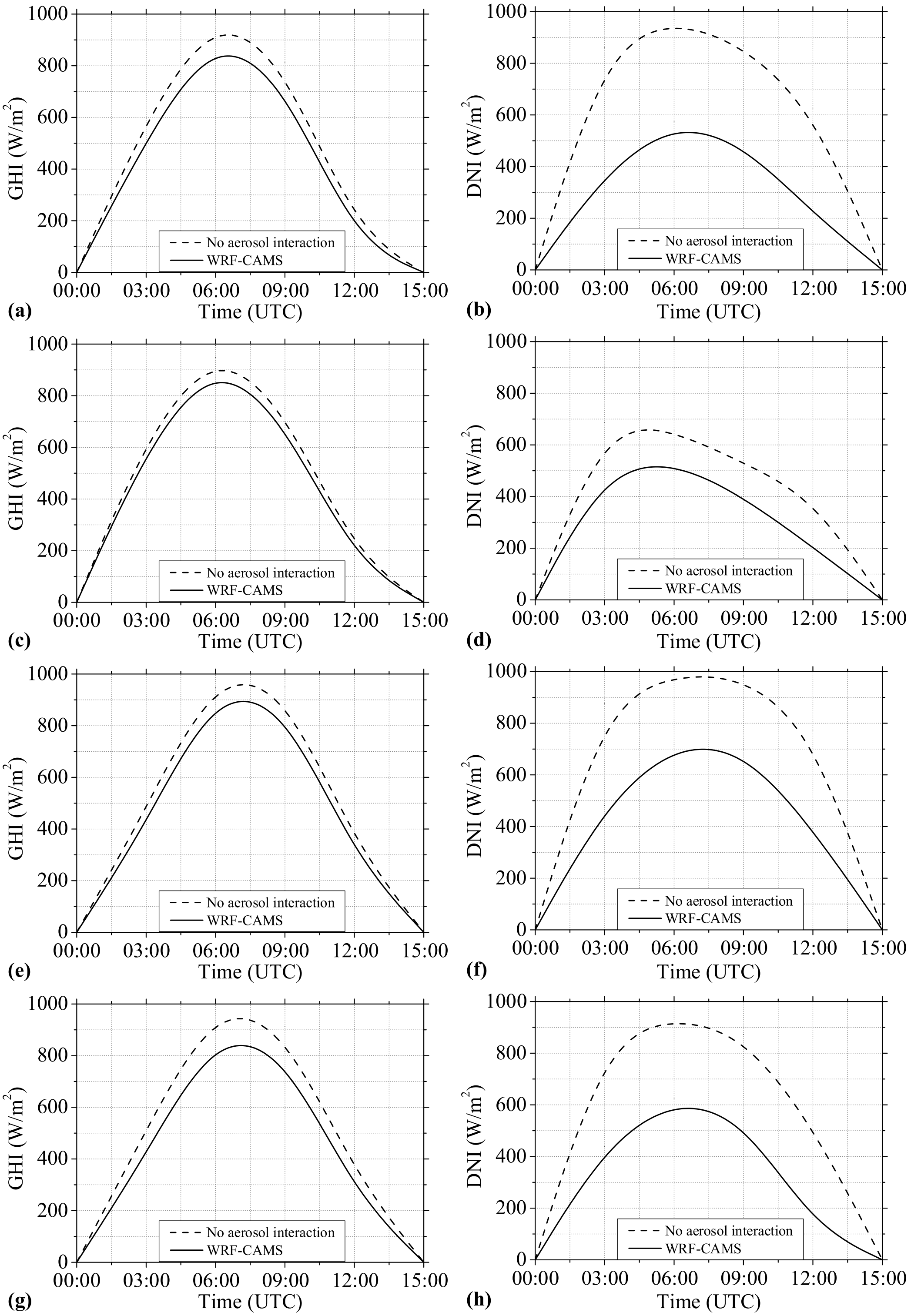

Fig. 13. Diurnal variation of GHI and DNI for north-west (a), north-east (b), south-west (c) and south-east (d) domains. WRF-CAMS corresponds to WRF prediction that includes aerosol-meteorology provided by CAMS. WRF0 corresponds to the scenario of no aerosol interaction when aerosol-meteorology is switched off in WRF runs.

in AOD, the impact on the irradiance simulations was found to be around 10% in most cases.

The BSRN GHI and DNI for the New Delhi station showed a lot more fluctuation in GHI as well as DNI on May 3, around 6 UTC than the other two days indicating the peak of the dust storm. Hence, the WRF simulations were performed for May 3, and the results showed that the dust event was captured accurately in WRF-CAMS runs. There was a significant reduction in the values of GHI and DNI in the northwestern region of the Indian subcontinent, showing the direct impact of the dust storm. There was a more pronounced decrease in the DNI values, reaching up to 600 W/m^2. The effect on the GHI ranged between 250 W/m^2 (at dust core) and 50 W/m^2 (on dust edges), which signifies that the solar energy exploitation in the areas of Rajasthan and Western Uttar Pradesh is immensely affected by drastic events such as the dust storms. The adverse effect of the dust plume on solar irradiance was seen from 03 to 12 UTC on May 3, 2018, which maximized at 07 UTC.

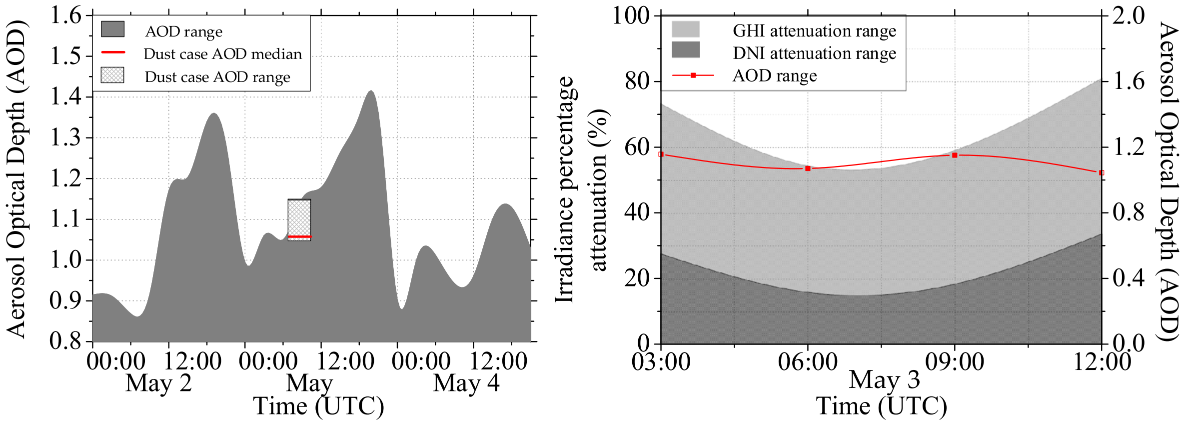

(a) (b)

Fig. 14. GHI and DNI percentage attenuation in New Delhi as a function of time of day and AOD. (a) 3 day range of AOD of CAMS near real-time forecasts and (b) percentage attenuation range for GHI and DNI as simulated by WRF. The shaded insert shows the corresponding median values and range at the peak of the strong dust incursion over the region on May 3, 2018.

The impact was more enhanced for the northwestern domain (Fig. 8a), where the maximum reduction in GHI and DNI was up to around 100 W/m^2 and 400 W/m^2, respectively, which corresponds to about 10% and 40% losses of GHI and DNI, respectively. For the investigation of the intensity of this dust case, a comparison was made between the attenuation in solar irradiance with the variation of AOD over New Delhi (IMD Delhi Aeronet site). The results showed significantly higher attenuation values around the local solar noon (which is around 07 UTC) and for DNI in general. In particular, at 07 UTC, the percentage decrease for GHI is around 15%, and for DNI 55%. At the same time, in the morning hours, the corresponding values are 28% and 74%, respectively, and in the evening hours, the corresponding values are 34% and 81%, respectively.

Declaration of competing interest

The authors declare that they have no known competing financial interests or personal relationships that could have appeared to influence the work reported in this paper.

Acknowledgments

P.K. acknowledges support by the EuroGEO e-shape project under grant agreement No. 820852 and by the Eiffel project under grant agreement No. 101003518. The MIDAS dataset has been developed in the framework of the DUST-GLASS project which has received funding from the European Union'os Horizon 2020 Research and Innovation program under the Marie Skłodowska-Curie grant agreement No. 749461. E.P. acknowledges support by the "PANhellenic infrastructure for Atmospheric Composition and climatE change" (MIS 5021516) project which is implemented under the Action "Reinforcement of the Research and Innovation Infrastructure", funded by the Operational Programme "Competitiveness, Entrepreneurship and Innovation" (NSRF 2014–2020) and co-financed by Greece and the European Union (European Regional Development Fund). A.G. acknowledges support by the ERC Consolidator Grant 2016 D-TECT: "Does dust TriboElectrification affect our ClimaTe" (grant no. 725698).

References

Akritidis, D., Antonakaki, T., Blechschmidt, A.-M., Clark, H., Gielen, C., Hendrick, F., Kapsomenakis, J., Kartsios, S., Katragkou, E., Melas, D., Mortier, A., Peters, E., Petersen, K., Piters, A., Richter, A., Van Roozendael, M., Schulz, M., Sudarchikova, N., Wagner, A., Zanis, P., Zerefos, C., 2017. Validation of the CAMS regional services: Concentrations above the surface. https://atmosphere.copernicus.eu/sites/default/files/2018-08/CAMS84_2015SC2_D84.5.1.8_D84.6.1.3_2017MAM_v1.pdf. (Accessed 30 September 2020).

Allen, R.J., Norris, J.R., Wild, M., 2013. Evaluation of multidecadal variability in CMIP5 surface solar radiation and inferred underestimation of aerosol direct effects over Europe, China, Japan, and India. J. Geophys. Res.: Atmos. 118, 6311–6336. http://dx.doi.org/10.1002/jgrd.50426.

Amiridis, V., Marinou, E., Tsekeri, A., Wandinger, U., Schwarz, A., Giannakaki, E., Mamouri, R., Kokkalis, P., Binietoglou, I., Solomos, S., Herekakis, T., Kazadzis, S., Gerasopoulos, E., Proestakis, E., Kottas, M., Balis, D., Papayannis, A., Kontoes, C., Kourtidis, K., Papagiannopoulos, N., Mona, L., Pappalardo, G., Rille, O.L., Ansmann, A., 2015. LIVAS: A 3-D multi-wavelength aerosol/cloud database based on CALIPSO and EARLINET. Atmos. Chem. Phys. 15, 7127–7153. http://dx.doi.org/10.5194/acp-15-7127-2015.

Amiridis, V., Wandinger, U., Marinou, E., Giannakaki, E., Tsekeri, A., Basart, S., Kazadzis, S., Gkikas, A., Taylor, M., Baldasano, J., Ansmann, A., 2013. Optimizing CALIPSO Saharan dust retrievals. Atmos. Chem. Phys. 13, 12089–12106. http://dx.doi.org/10.5194/acp-13-12089-2013.

Aswini, M.A., Kumar, A., Das, S.K., 2020. Quantification of long-range transported aeolian dust towards the Indian peninsular region using satellite and ground-based data - A case study during a dust storm over the Arabian sea. Atmos. Res. 239, 104910. http://dx.doi.org/10.1016/j.atmosres.2020.104910.

Baars, H., Kanitz, T., Engelmann, R., Althausen, D., Heese, B., Komppula, M., Preißler, J., Tesche, M., Ansmann, A., Wandinger, U., Lim, J.-H., Ahn, J.Y., Stachlewska, I.S., Amiridis, V., Marinou, E., Seifert, P., Hofer, J., Skupin, A., Schneider, F., Bohlmann, S., Foth, A., Bley, S., Pfüller, A., Giannakaki, E., Lihavainen, H., Viisanen, Y., Hooda, R.K., Pereira, S.N., Bortoli, D., Wagner, F., Mattis, I., Janicka, L., Markowicz, K.M., Achtert, P., Artaxo, P., Pauliquevis, T., Souza, R.A.F., Sharma, V.P., van Zyl, P.G., Beukes, J.P., Sun, J., Rohwer, E.G., Deng, R., Mamouri, R.-E., Zamorano, F., 2016. An overview of the first decade of $POLLY^{Net}$: An emerging network of automated Raman-polarization lidars for continuous aerosol profiling. Atmos. Chem. Phys. 16, 5111–5137. http://dx.doi.org/10.5194/acp-16-5111-2016.

Basart, S., Benedictow, A., Bennouna, Y., Blechschmidt, A.M., Chabrillat, S., Clark, H., Cuevas, E., Flentje, H., Hansen, K.M., Im, U., Kapsomenakis, J., Langerock, B., Richter, A., Sudarchikova, N., Thouret, V., Warneke, T., Zerefos, C., 2019. Validation report of the CAMS near-real-time global atmospheric composition service. pp. 1–168. http://dx.doi.org/10.24380/322n-jn39.

Benedetti, A., Morcrette, J.-J., Boucher, O., Dethof, A., Engelen, R., Fisher, M., Flentjes, H., Huneeus, N., Jones, L., Kaiser, J., Kinne, S., Mangold, A., Razinger, M., Simmons, A., Suttie, M., the GEMS-A.E.R. team, 2008. Aerosol analysis and forecast in the ECMWF Integrated Forecast System: Data assimilation. J. Geophys. Res. 571, 1–23. http://dx.doi.org/10.21957/g3bogeske.

Cavallo, S.M., Dudhia, J., Snyder, C., 2010. A multilayer upper-boundary condition for longwave radiative flux to correct temperature biases in a mesoscale model. Mon. Weather Rev. 139, 1952–1959. http://dx.doi.org/10.1175/2010MWR3513.1.

Chakravarty, K., Vincent, V., Vellore, R., Srivastava, A.K., Rastogi, A., Soni, V.K., 2021. Revisiting Andhi in northern India: A case study of severe dust-storm over the urban megacity of New Delhi. Urban Clim. 37, 100825. http://dx.doi.org/10.1016/j.uclim.2021.100825.

Charabi, Y., Gastli, A., 2012. Spatio-temporal assessment of dust risk maps for solar energy systems using proxy data. Renew. Energy 44, 23–31. http://dx.doi.org/10.1016/j.renene.2011.12.005.

Chen, S., Huang, J., Kang, L., Wang, H., Ma, X., He, Y., Yuan, T., Yang, B., Huang, Z., Zhang, G., 2017. Emission, transport, and radiative effects of mineral dust from the Taklimakan and Gobi deserts: Comparison of measurements and model results. Atmos. Chem. Phys. 17, 2401–2421. http://dx.doi.org/10.5194/acp-17-2401-2017.

Clough, S.A., Iacono, M.J., Moncet, J.-luc, 1992. Line-by-line calculations of atmospheric fluxes and cooling rates: Application to water vapor. J. Geophys. Res. 97, 15761–15785. http://dx.doi.org/10.1029/92JD01419.

Dee, D.P., Uppala, S., 2009. Variational bias correction of satellite radiance data in the ERA-Interim reanalysis. Q. J. R. Meteorol. Soc. 135, 1830–1841. http://dx.doi.org/10.1002/qj.493.

Deepshikha, S., Satheesh, S.K., Srinivasan, J., 2005. Regional distribution of absorbing efficiency of dust aerosols over India and adjacent continents inferred using satellite remote sensing. Geophys. Res. Lett. 32, 1–4. http://dx.doi.org/10.1029/2004GL022091.

Dey, S., Tripathi, S.N., Singh, R.P., Holben, B.N., 2004. Influence of dust storms on the aerosol optical properties over the Indo-Gangetic basin. J. Geophys. Res. D 109, 1–13. http://dx.doi.org/10.1029/2004JD004924.

Dirnberger, D., Blackburn, G., Muller, B., Reise, C., 2015. On the impact of solar spectral irradiance on the yield of different PV technologies. Sol. Energy Mater. Sol. Cells 118, 6311–6336. http://dx.doi.org/10.1016/j.solmat.2014.09.034.

Du, Y., Xu, X., Chu, M., Guo, Y., Wang, J., 2016. Air particulate matter and cardiovascular disease: The epidemiological, biomedical and clinical evidence. J. Thoraic Dis. 8, 8–19. http://dx.doi.org/10.3978/j.issn.2072-1439.2015.11.37.

Dubovik, O., Smirnov, A., Holben, B.N., King, M.D., Kaufman, Y.J., Eck, T.F., Slutsker, I., 2000. Accuracy assessments of aerosol optical properties retrieved from Aerosol Robotic Network (AERONET) Sun and sky radiance measurements. J. Geophys. Res.: Atmos. 105, 9791–9806. http://dx.doi.org/10.1029/2000JD900040.

Earlinet, 2020. A European aerosol research lidar network to establish an aerosol climatology: EARLINET. https://www.earlinet.org/index.php?id=earlinet_homepage. (Accessed 17 July 2020).

Engelen, R., 2018. CAMS service product portfolio. https://atmosphere.copernicus.eu/sites/default/files/2018-11/2_Engelen_Portfolio_2018.pdf. (Accessed 20 December 2020).

Eskes, H., Huijnen, V., Arola, A., Benedictow, A., Blechschmidt, A.M., Botek, E., Boucher, O., Bouarar, I., Chabrillat, S., Cuevas, E., Engelen, R., Flentje, H., Gaudel, A., Griesfeller, J., Jones, L., Kapsomenakis, J., Katragkou, E., Kinne, S., Langerock, B., Razinger, M., Richter, A., Schultz, M., Schulz, M., Sudarchikova, N., Thouret, V., Vrekoussis, M., Wagner, A., Zerefos, C., 2015. Validation of reactive gases and aerosols in the MACC global analysis and forecast system. Geosci. Model Dev. 8, 3523–3543. http://dx.doi.org/10.5194/gmd-8-3523-2015.

Filioglou, M., Giannakaki, E., Backman, J., Kesti, J., Hirsikko, A., Engelmann, R., O'Connor, E., Leskinen, J.T.T., Shang, X., Korhonen, H., Lihavainen, H., Romakkaniemi, S., Komppula, M., 2020. Optical and geometrical aerosol particle properties over the United Arab Emirates. Atmos. Chem. Phys. 20, 8909—8922. http://dx.doi.org/10.5194/acp-2020-133.

Francis, D., Chaboureau, J.P., Nelli, N., Cuesta, J., Alshamsi, N., Temimi, M., Pauluis, O., Xue, L., 2021. Summertime dust storms over the Arabian Peninsula and impacts on radiation, circulation, cloud development and rain. Atmos. Res. 250, 105364. http://dx.doi.org/10.1016/j.atmosres.2020.105364.

Gelaro, R., McCarty, W., Suárez, M.J., Todling, R., Molod, A., Takacs, L., Randles, C.A., Darmenov, A., Bosilovich, M.G., Reichle, R., Wargan, K., Coy, L., Cullather, R., Draper, C., Akella, S., Buchard, V., Conaty, A., da Silva, A.M., Gu, W., Kim, G.-K., Koster, R., Lucchesi, R., Merkova, D., Nielsen, J.E., Partyka, G., Pawson, S., Putman, W., Rienecker, M., Schubert, S.D., Sienkiewicz, M., Zhao, B., 2017. The modern-era retrospective analysis for research and applications, version 2 (MERRA-2). J. Clim. 30, 5419–5454. http://dx.doi.org/10.1175/JCLI-D-16-0758.1.

Gkikas, A., Proestakis, E., Amiridis, V., Kazadzis, S., Di Tomaso, E., Tsekeri, A., Marinou, E., Hatzianastassiou, N., Pérez García-Pando, C., 2021. ModIs dust AeroSol (MIDAS): A global fine-resolution dust optical depth data set. Atmos. Meas. Tech. 14, 309–334. http://dx.doi.org/10.5194/amt-14-309-2021.

Gschwind, B., Wald, L., Blanc, P., Lefèvre, M., Schroedter-Homscheidt, M., Arola, A., 2019. Improving the McClear model estimating the downwelling solar radiation at ground level in cloud-free conditions – McClear-v3. Meteorol. Z. 28, 147–163. http://dx.doi.org/10.1127/metz/2019/0946.

Holben, B.N., Tanré, D., Smirnov, A., Eck, T.F., Slutsker, I., Abuhassan, N., Newcomb, W.W., Schafer, J.S., Chatenet, B., Lavenu, F., Kaufman, Y.J., Castle, J.V., Setzer, A., Markham, B., Clark, D., Frouin, R., Halthore, R., Karneli, A., O'Neill, N.T., Pietras, C., Pinker, R.T., Voss, K., Zibordi, G., 2001. An emerging ground-based aerosol climatology: Aerosol optical depth from AERONET. J. Geophys. Res.: Atmos. 106, 12067–12097. http://dx.doi.org/10.1029/2001JD900014.

Hou, Y.-T., Moorthi, S., Campana, K., 2002. Parameterization of Solar Radiation Transfer in the NCEP Models. National Centers for Environmental Prediction, https://repository.library.noaa.gov/view/noaa/23085.

Huang, C.C., Chen, S.H., Lin, Y.C., Earl, K., Matsui, T., Lee, H.H., Tsai, I.C., Chen, J.P., Cheng, C.T., 2019. Impacts of dust-radiation versus dust-cloud interactions on the development of a modeled mesoscale convective system over North Africa. Mon. Weather Rev. 147, 3301–3326. http://dx.doi.org/10.1175/MWR-D-18-0459.1.

Huang, Z., Huang, J., Hayasaka, T., Wang, S., Zhou, T., Jin, H., 2015. Short-cut transport path for Asian dust directly to the Arctic: A case study. Environ. Res. Lett. 10, 114018. http://dx.doi.org/10.1088/1748-9326/10/11/114018.

Huang, J., Minnis, P., Yi, Y., Tang, Q., Wang, X., Hu, Y., Liu, Z., Ayers, K., Trepte, C., Winker, D., 2007. Summer dust aerosols detected from CALIPSO over the Tibetan Plateau. Geophys. Res. Lett. 34, 1–5. http://dx.doi.org/10.1029/2007GL029938.

Iacono, M.J., Delamere, J.S., Mlawer, E.J., Shephard, M.W., Clough, S.A., Collins, W.D., 2008. Radiative forcing by long-lived greenhouse gases: Calculations with the AER radiative transfer models. J. Geophys. Res. 113, 2–9. http://dx.doi.org/10.1029/2008JD009944.

ISRO, 2015. INSAT-3D: Algorithm theoretical basis development document. https://mosdac.gov.in/data/doc/INSAT_3D_ATBD_MAY_2015.pdf. (Accessed 20 December 2020).

Janjic, Z.I., 1990. The step-mountain coordinate: Physical package. Mon. Weather Rev. 118, 1429–1443. http://dx.doi.org/10.1175/1520-0493(1990)118<1429:TSMCPP>2.0.CO;2.

Jin, H., Yi, Y., Nasiri, S.L., Liu, C., Wang, W., Li, J., Chen, Y., 2015. Impacts of Asian dust on the determination of cloud thermodynamic phase from satellite observations impacts of Asian dust on the determination of cloud thermodynamic phase from satellite observations. Environ. Res. Lett. 10, 34006. http://dx.doi.org/10.1088/1748-9326/10/3/034006.

Kedia, S., Kumar, R., Islam, S., Sathe, Y., Kaginalkar, A., 2018. Radiative impact of a heavy dust storm over India and surrounding oceanic regions. Atmos. Environ. 185, 109–120. http://dx.doi.org/10.1016/j.atmosenv.2018.05.005.

Kosmopoulos, P.G., Kazadzis, S., El-Askary, H., Taylor, M., Gkikas, A., Proestakis, E., Kontoes, C., El-Khayat, M.M., 2018a. Earth-observation-based estimation and forecasting of particulate matter impact on solar energy in Egypt. Remote Sens. 10, 1870. http://dx.doi.org/10.3390/rs10121870.

Kosmopoulos, P.G., Kazadzis, S., Lagouvardos, K., Kotroni, V., Bais, A., 2015. Solar energy prediction and verification using operational model forecasts and ground-based solar measurements. Energy 93, 1918–1930. http://dx.doi.org/10.1016/j.energy.2015.10.054.

Kosmopoulos, P.G., Kazadzis, S., Taylor, M., Athanasopoulou, E., Speyer, O., Raptis, P.I., Marinou, E., Proestakis, E., Solomos, S., Gerasopoulos, E., Amiridis, V., Bais, A., Kontoes, C., 2017a. Dust impact on surface solar irradiance assessed with model simulations, satellite observations and ground-based measurements. Atmos. Meas. Tech. 10, 1–32. http://dx.doi.org/10.5194/amt-2017-79.

Kosmopoulos, P.G., Kazadzis, S., Taylor, M., Bais, A.F., Lagouvardos, K., Kotroni, V., Keramitsoglou, I., Kiranoudis, C., 2017b. Estimation of the solar energy potential in Greece using satellite and ground-based observations. In: Karacostas, T., Bais, A., Nastos, P.T. (Eds.), Perspectives on Atmospheric Sciences. Springer International Publishing, Cham, pp. 1149–1156. http://dx.doi.org/10.1007/978-3-319-35095-0_165.

Kosmopoulos, P.G., Kazadzis, S., Taylor, M., Raptis, P.I., Keramitsoglou, I., Kiranoudis, C., Bais, A.F., 2018b. Assessment of surface solar irradiance derived from real-time modelling te chniques and verification with ground-based measurements. Atmos. Meas. Tech. 11, 907–924. http://dx.doi.org/10.5194/amt-11-907-2018.

Kumar, S., Kumar, S., Kaskaoutis, D.G., Singh, R.P., Singh, R.K., Mishra, A.K., Srivastava, M.K., Singh, A.K., 2015. Meteorological, atmospheric and climatic perturbations during major dust storms over Indo-Gangetic basin. Aeolian Res. 17, 15–31. http://dx.doi.org/10.1016/j.aeolia.2015.01.006.

Langerock, B., De Mazière, M., Hendrick, F., Vigouroux, C., Desmet, F., Dils, B., Niemeijer, S., 2015. Description of algorithms for co-locating and comparing gridded model data with remote-sensing observations. Geosci. Model Dev. 8, 911–921. http://dx.doi.org/10.5194/gmd-8-911-2015.

Levy, R.C., Mattoo, S., Munchak, L.A., Remer, L.A., Sayer, A.M., Patadia, F., Hsu, N.C., 2013. The Collection 6 MODIS aerosol products over land and ocean. Atmos. Meas. Tech. 6, 2989–3034. http://dx.doi.org/10.5194/amt-6-2989-2013.

Lindfors, A.V., Kouremeti, N., Arola, A., Kazadzis, S., Bais, A.F., Laaksonen, A., 2013. Effective aerosol optical depth from pyranometer measurements of surface solar radiation (global radiation) at Thessaloniki, Greece. Atmos. Chem. Phys. 13, 3733–3741. http://dx.doi.org/10.5194/acp-13-3733-2013.

Lozano, J.A.M., Utrillas, M.P., Tena, F., Cachorro, V.E., 1998. The parameterisation of the atmospheric aerosol optical depth using the Angstrom power law. Sol. Energy 63, 303–311. http://dx.doi.org/10.1016/S0038-092X(98)00077-2.

Marinou, E., Amiridis, V., Binietoglou, I., Tsikerdekis, A., Solomos, S., Proestakis, E., Konsta, D., Papagiannopoulos, N., Tsekeri, A., Vlastou, G., Zanis, P., Balis, D., Wandinger, U., Ansmann, A., 2017. Three-dimensional evolution of Saharan dust transport towards Europe based on a 9-year EARLINET-optimized CALIPSO dataset. Atmos. Chem. Phys. 17, 5893–5919. http://dx.doi.org/10.5194/acp-17-5893-2017.

Masoom, A., Kashyap, Y., Bansal, A., 2019. Solar radiation assessment and forecasting using satellite data. In: Tyagi, H., Agarwal, A.K., Chakraborty, P.R., Powar, S. (Eds.), Advances in Solar Energy Research. Springer Singapore, Singapore, pp. 45–71. http://dx.doi.org/10.1007/978-981-13-3302-6_3.

Masoom, A., Kosmopoulos, P., Bansal, A., Kazadzis, S., 2020a. Solar energy estimations in India using remote sensing technologies and validation with sun photometers in urban areas. Remote Sens. 12, 254. http://dx.doi.org/10.3390/rs12020254.

Masoom, A., Kosmopoulos, P., Kashyap, Y., Kumar, S., Bansal, A., 2020b. Rooftop photovoltaic energy production management in India using Earth-observation data and modeling techniques. Remote Sens. 12, 1921. http://dx.doi.org/10.3390/rs12121921.

Mellor, G.L., Yamada, T., 1982. Development of a turbulence closure model for geophysical fluid problems. Rev. Geophys. 20, 851–875. http://dx.doi.org/10.1029/RG020i004p00851.

Middleton, N.J., 1986. A geography of dust storms in South-West Asia. J. Climatol. 6, 183–196. http://dx.doi.org/10.1002/joc.3370060207.

Miller, R.L., Tegen, I., Perlwitz, J., 2004. Surface radiative forcing by soil dust aerosols and the hydrologic cycle. J. Geophys. Res.: Atmos. 109, 1–24. http://dx.doi.org/10.1029/2003JD004085.

Mlawer, E.J., Clough, S.A., 1998. Shortwave and longwave enhancements in the rapid radiative transfer model. In: Proceedings of the Seventh Atmospheric Radiation Measurement, ARM Science Team Meeting. pp. 409–413, https://www.arm.gov/publications/proceedings/conf07/extended_abs/mlawer_ej.pdf.

Mlawer, E.J., Taubman, S.J., Brown, P.D., Iacono, M.J., Clough, S.A., 1997. Radiative transfer for inhomogeneous atmospheres: RRTM, a validated correlated-k model for the longwave. J. Geophys. Res.: Atmos. 102, 16663–16682. http://dx.doi.org/10.1029/97JD00237.

Morcrette, J.J., Beljaars, A., Benedetti, A., Jones, L., Boucher, O., 2008. Sea-salt and dust aerosols in the ECMWF IFS model. Geophys. Res. Lett. 35, 1–5. http://dx.doi.org/10.1029/2008GL036041.

Mosdac, 2020. Meteorological & oceanographic satellite data archival centre. https://www.mosdac.gov.in/. (Accessed 08 June 2018).

NASA, 2020. LAADS DAAC. https://ladsweb.modaps.eosdis.nasa.gov/. (Accessed 17 August 2020).

NCEP, 2015. NCEP GFS 0.25 Degree Global Forecast Grids Historical Archive. Research Data Archive at the National Center for Atmospheric Research, Computational and Information Systems Laboratory, Boulder, CO, http://dx.doi.org/10.5065/D65D8PWK.

Ohde, T., Siegel, H., 2012. Impacts of Saharan dust and clouds on photosynthetically available radiation in the area off Northwest Africa. Tellus B 64, 17160. http://dx.doi.org/10.3402/tellusb.v64i0.17160.

O'Neill, N.T., Eck, T.F., Smirnov, A., Holben, B.N., Thulasiraman, S., 2003. Spectral discrimination of coarse and fine mode optical depth. J. Geophys. Res.: Atmos. 108, 1–15. http://dx.doi.org/10.1029/2002jd002975.

Papayannis, A., Balis, D., Amiridis, V., Chourdakis, G., Tsaknakis, G., Zerefos, C., Castanho, A.D.A., Nickovic, S., Kazadzis, S., Grabowski, J., 2005. Measurements of Saharan dust aerosols over the eastern Mediterranean using elastic backscatter-Raman lidar, spectrophotometric and satellite observations in the frame of the EARLINET project. Atmos. Chem. Phys. 5, 2065–2079. http://dx.doi.org/10.5194/acp-5-2065-2005.

Pappalardo, G., Amodeo, A., Apituley, A., Comeron, A., Freudenthaler, V., Linné, H., Ansmann, A., Bösenberg, J., D'Amico, G., Mattis, I., Mona, L., Wandinger, U., Amiridis, V., Alados-Arboledas, L., Nicolae, D., Wiegner, M., 2014. EARLINET: Towards an advanced sustainable European aerosol lidar network. Atmos. Meas. Tech. 7, 2389–2409. http://dx.doi.org/10.5194/amt-7-2389-2014.

Paulescu, M., Schlett, Z., 2003. A simplified but accurate spectral solar irradiance model. Theor. Appl. Climatol. 75, 203–212. http://dx.doi.org/10.1007/s00704-003-0731-y.

Perez, R., Lorenz, E., Pelland, S., Beauharnois, M., Van Knowe, G., Hemker, K., Heinemann, D., Remund, J., Müller, S.C., Traunmüller, W., Steinmauer, G., Pozo, D., Ruiz-Arias, J.A., Lara-Fanego, V., Ramirez-Santigosa, L., Gaston-Romero, M., Pomares, L.M., 2013. Comparison of numerical weather prediction solar irradiance forecasts in the US, Canada and Europe. Sol. Energy 94, 305–326. http://dx.doi.org/10.1016/j.solener.2013.05.005.

Prasad, A.K., Singh, R.P., 2007. Changes in aerosol parameters during major dust storm events (2001–2005) over the Indo-Gangetic plains using AERONET and MODIS data. J. Geophys. Res.: Atmos. 112, 1–18. http://dx.doi.org/10.1029/2006JD007778.

Proestakis, E., Amiridis, V., Marinou, E., Georgoulias, A.K., Solomos, S., Kazadzis, S., Chimot, J., Che, H., Alexandr, G., Binietoglou, I., Daskalopoulou, V., Kourtidis, K.A., de Leeuw, G., van der A, R.J., 2018. Nine-year spatial and temporal evolution of desert dust aerosols over South and East Asia as revealed by CALIOP. Atmos. Chem. Phys. 18, 1337–1362. http://dx.doi.org/10.5194/acp-18-1337-2018.

Qian, Y., Wang, W., Leung, L.R., Kaiser, D.P., 2007. Variability of solar radiation under cloud-free skies in China: The role of aerosols. Geophys. Res. Lett. 34, 1–5. http://dx.doi.org/10.1029/2006GL028800.

Ramanathan, K., 2019. Basic Measurements of Radiation at Station Gurgaon (2018-05). National Institute of Wind Energy, http://dx.doi.org/10.1594/PANGAEA.897832.

Reddy, M.S., Boucher, O., Bellouin, N., Schulz, M., Balkanski, Y., Dufresne, J.-L., Pham, M., 2005. Estimates of global multicomponent aerosol optical depth and direct radiative perturbation in the laboratoire de Météorologie dynamique general circulation model. J. Geophys. Res. D 110, 1–16. http://dx.doi.org/10.1029/2004JD004757.

Salomonson, V.V., Barnes, W.L., Maymon, P.W., Montgomery, H.E., Ostrow, H., 1989. MODIS: Advanced facility instrument for studies of the Earth as a system. IEEE Trans. Geosci. Remote Sens. 27, 145–153. http://dx.doi.org/10.1109/36.20292.

Sarkar, S., Chauhan, A., Kumar, R., Singh, R.P., 2019. Impact of deadly dust storms (May 2018) on air quality, meteorological, and atmospheric parameters over the northern parts of India. GeoHealth 3, 67–80. http://dx.doi.org/10.1029/2018gh000170.

Schroedter-Homscheidt, M., Oumbe, A., Benedetti, A., Morcrette, J.J., 2013. Aerosols for concentrating solar electricity production forecasts: Requirement quantification and ECMWF/MACC aerosol forecast assessment. Bull. Am. Meteorol. Soc. 94, 903–914. http://dx.doi.org/10.1175/BAMS-D-11-00259.1.

Sikka, D.R., 1997. Desert climate and its dynamics. Current Sci. 72, 35–46, URL http://www.jstor.org/stable/24098628.

Skamarock, W.C., Klemp, J.B., Dudhia, J., Gill, D.O., Barker, D.M., Duda, M.G., Huang, X.-Y., Wang, W., Powers, J.G., 2008. A Description of the Advanced Research WRF Version 3. NCAR Technical Note, University Corporation for Atmospheric Research, http://dx.doi.org/10.5065/D68S4MVH.

Slingo, A., Ackerman, T.P., Allan, R.P., Kassianov, E.I., McFarlane, S.A., Robinson, G.J., Barnard, J.C., Miller, M.A., Harries, J.E., Russell, J.E., Dewitte, S., 2006. Observations of the impact of a major Saharan dust storm on the atmospheric radiation balance. Geophys. Res. Lett. 33, 3–7. http://dx.doi.org/10.1029/2006GL027869.

Stanelle, T., Vogel, B., Vogel, H., Bäumer, D., Kottmeier, C., 2010. Feedback between dust particles and atmospheric processes over West Africa during dust episodes in March 2006 and June 2007. Atmos. Chem. Phys. 10, 10771–10788. http://dx.doi.org/10.5194/acp-10-10771-2010.

Stephens, G.L., Greenwald, T.J., 1991. The Earth's radiation budget and its relation to atmospheric hydrology: 2. Observations of cloud effects. J. Geophys. Res. 96, 15325–15340. http://dx.doi.org/10.1029/91jd00972.

Tackett, J.L., Winker, D.M., Getzewich, B.J., Vaughan, M.A., Young, S.A., Kar, J., 2018. CALIPSO lidar level 3 aerosol profile product: Version 3 algorithm design. Atmos. Meas. Tech. 11, 4129–4152. http://dx.doi.org/10.5194/amt-11-4129-2018.

Tegen, I., Hollrig, P., Chin, M., Fung, I., Jacob, D., Penner, J., 1997. Contribution of different aerosol species to the global aerosol extinction optical thickness: Estimates from model results. J. Geophys. Res. 102, 23895–23915. http://dx.doi.org/10.1029/97JD01864.

Tesche, M., Ansmann, A., Müller, D., Althausen, D., Engelmann, R., Freudenthaler, V., Groß, S., 2009. Vertically resolved separation of dust and smoke over Cape Verde using multiwavelength Raman and polarization lidars during Saharan mineral dust experiment 2008. J. Geophys. Res.: Atmos. 114, 1–14. http://dx.doi.org/10.1029/2009JD011862.

Thompson, G., Field, P.R., Rasmussen, R.M., Hall, W.D., 2008. Explicit forecasts of winter precipitation using an improved bulk microphysics scheme. Part II: Implementation of a new snow parameterization. Mon. Weather Rev. 136, 5095–5115. http://dx.doi.org/10.1175/2008MWR2387.1.

Tiedtke, M., 1989. A comprehensive mass flux scheme for cumulus parameterization in large-scale models. Mon. Weather Rev. 117, 1779–1800. http://dx.doi.org/10.1175/1520-0493(1989)117<1779:ACMFSF>2.0.CO;2.

Vaughan, M.A., Powell, K.A., Winker, D.M., Hostetler, C.A., Kuehn, R.E., Hunt, W.H., Getzewich, B.J., Young, S.A., Liu, Z., McGill, M.J., 2009. Fully automated detection of cloud and aerosol layers in the CALIPSO lidar measurements. J. Atmos. Ocean. Technol. 26, 2034–2050. http://dx.doi.org/10.1175/2009JTECHA1228.1.

Verma, S., Payra, S., Gautam, R., Prakash, D., Soni, M., Holben, B., Bell, S., 2013. Dust events and their influence on aerosol optical properties over Jaipur in Northwestern India. Environ. Monit. Assess. 185, 7327–7342. http://dx.doi.org/10.1007/s10661-013-3103-9.

Vogel, B., Hoose, C., Vogel, H., Kottmeier, C., 2006. A model of dust transport applied to the Dead Sea area. Meteorol. Z. 15, 611–624. http://dx.doi.org/10.1127/0941-2948/2006/0168.

Wang, T., Han, Y., Huang, J., 2020a. Climatology of Dust - forced radiative heating over the Tibetan plateau and its surroundings. 125, 1–14. http://dx.doi.org/10.1029/2020JD032942.

Wang, T., Tang, J., Sun, M., Liu, X., Huang, Y., Huang, J., Han, Y., Cheng, Y., Huang, Z., Li, J., 2020b. Identifying a transport mechanism of dust aerosols over South Asia to the Tibetan plateau: A case study. Sci. Total Environ. 758, 143714. http://dx.doi.org/10.1016/j.scitotenv.2020.143714.

Wang, P., van Westrhenen, R., Meirink, J.F., van der Veen, S., Knap, W., 2019. Surface solar radiation forecasts by advecting cloud physical properties derived from Meteosat second generation observations. Sol. Energy 177, 47–58. http://dx.doi.org/10.1016/j.solener.2018.10.073.

Winker, D.M., Hunt, W.H., McGill, M.J., 2007. Initial performance assessment of CALIOP. Geophys. Res. Lett. 34, 1–5. http://dx.doi.org/10.1029/2007GL030135.

Yuan, T., Huang, J., Cao, J., Zhang, G., Ma, X., 2021. Indian dust-rain storm: Possible influences of dust ice nuclei on deep convective clouds. Sci. Total Environ. 779, 146439. http://dx.doi.org/10.1016/j.scitotenv.2021.146439.